BRNO UNIVERSITY OF TECHNOLOGY

VYSOKÉ UČENÍ TECHNICKÉ V BRNĚ

FACULTY OF MECHANICAL ENGINEERING

FAKULTA STROJNÍHO INŽENÝRSTVÍ

INSTITUTE OF PHYSICAL ENGINEERING

ÚSTAV FYZIKÁLNÍHO INŽENÝRSTVÍ

ADVANCEMENTS OF HOLOGRAPHIC ENDOSCOPY FOR IN-VIVO OBSERVATIONS

POKROČILÁ HOLOGRAFICKÁ ENDOSKOPIE PRO POZOROVÁNÍ IN-VIVO

MASTER'S THESIS

DIPLOMOVÁ PRÁCE

AUTOR PRÁCE
AUTHOR

Bc. IVANA MICHÁLKOVÁ

SUPERVISOR
VEDOUCÍ PRÁCE

prof. Mgr. TOMÁŠ ČIŽMÁR, Ph.D.

BRNO 2023

Summary

In recent years, a novel technique called holographic endoscopy has been developed and systematically improved. This unique technology utilizes a single hair-thin optical multimode fiber as a minimally invasive probe for deep tissue in vivo microscopy.

A major milestone was reached last year when near-perfect focusing through a multimode fiber was achieved with the holographic endoscope. This breakthrough is significant for adapting scanning fluorescent microscopy techniques because it allows for more precise imaging with lower unwanted noise, thanks to the purity and fidelity of the focused excitation light.

The achievement led to a new question: is it possible to generate more complex optical fields than diffraction-limited foci through the multimode fiber with comparable quality? This thesis aims to investigate this issue by producing Airy beams at the tip of the multimode fiber using the holographic endoscope setup. Two methods were used to produce Airy beams in this study: Fourier domain and direct field synthesis. The quality of the resulting beams was evaluated by comparing them to simulations. The propagation of the generated beams was also recorded and observed, and the potential of Fourier domain synthesis to control and modify the propagation characteristics of an Airy beam was explored.

The analysis revealed that using the holographic endoscope setup, it is possible to create more complex optical fields, such as Airy beams, at the tip of a multimode fiber with an accuracy that matches the high-quality diffraction-limited foci produced in 2022.

It is hoped that this work will serve as another stepping stone for the holographic endoscope's ability to work in microscopy regimes that utilize more complex light fields, such as structured illumination microscopy or stimulated emission depletion microscopy.

Abstrakt

Počas posledných rokov bola vyvinutá a systematicky vylepšovaná nová unikátna technológia zvaná holografická endoskopia. Táto jedinečná metóda využíva jediné multimodálne optické vlákno, o hrúbke ľudského vlasu, ako minimálne invazívnu sondu pre mikroskopické zobrazovanie v hĺbke živých tkanív. Minulý rok sa dosiahlo ďalšieho pokroku, pričom sa vďaka holografickému endoskopu podarilo vytvoriť takmer perfektné difrakciou limitované body na konci multimodálneho vlákna. Tieto výsledky sú dôležité najmä z hľadiska využitia skenovacích florescenčných mikroskopických metód vrámci zobrazovania pomocou holografického endoskopu, pretože lepšia kvalita excitačného svetla umožňuje presnejšie zobrazovania s obmedzením tvorby nežiadúcich signálov.

Spomenuté výsledky viedli k novej otázke: Bolo by možné vytvoriť cez multimodálne optické vlákno aj komplexnejšie svetelné polia než sú difrakciou limitované body, so zachovaním vysokej kvality? Jedným z hlavných cieľov tejto diplomovej práce bolo preskúmať túto možnosť, tvorbou Airyho zväzkov cez multimodálne vlákno s využitím holografického endoskopu.

Pre generovanie Airyho zväzkov boli použité dve metódy: syntéza pomocou fázovej masky a priama syntéza. Kvalita vytvorených zväzkov bola určená ich porovnaním so simuláciou. Okrem toho bola zaznamenaná aj propagácia jednotlivých zväzkov a preskúmaný potenciál syntézy pomocou fázovej masky, pre ovplyvňovanie propagačných charakteristík Airyho zväzku.

Analýza výsledkov ukázala, že s využitím holografického endoskopu je možné cez multimodálne optické vlákno vytvoriť aj komplexnejšie polia, ako napr. Airyho zväzok, a

to s presnosťou zodpovedajúcou vysokokvalitným difrakciou limitovaným bodom vygenerovaným v roku 2022.

Táto práca snáď poskytne ďalší míľnik vo vývoji holografickej endoskopie, konkrétne k schopnosti holografického endoskopu pracovať v mikroskopických režimoch využívajúcich zložitejšie optické polia ako je napr. SIM či STED mikroskopia.

Keywords
holographic endoscopy, multimode optical fibre, complex media photonics, transformation matrix theory, digital spatial light modulation, Gaussian beam, Airy beam

Klíčová slova
holografická endoskopia, multimodálne optické vlákno, fotonika rozptyľujúcich prostredí, prenosová matica, digitálna modulácia svetla, Gaussovský zväzok, Airyho zväzok

MICHÁLKOVÁ, I. *Advancements of Holographic endoscopy for in-vivo observations.* Brno: University of technology in Brno, Faculty of Mechanical Engineering, 2023. 38 s. Vedoucí prof. Mgr. Tomáš Čižmár, Ph.D.

I declare that the master thesis submitted hereby is my own work under the supervision of Prof. Mgr. Tomáš Čižmár, Ph.D., and Dr. André D. Gomes and that all literature sources were quoted completely and correctly.

Bc. Ivana Michálková

I would like to express my sincere gratitude to all those who have supported me throughout my academic journey. Without their help, guidance, and encouragement, I would not have been able to complete this master's thesis. First and foremost, I want to thank my supervisor, Prof. Mgr. Tomáš Čižmár, Ph.D., for his invaluable guidance during the writing process. His thoughtful feedback and expert advice were instrumental in shaping this thesis. I would also like to extend my heartfelt thanks to Dr. André D. Gomes, who supported and supervised me during my Erasmus stay with a kind and patient approach. His expertise and mentorship were indispensable to this project. I am also grateful to Simone Colombel and all the members of the Holographic endoscopy group at Leibniz Institute of Photonic Technologies for creating a supportive and friendly atmosphere during my stay there.

Finally, I want to thank my family and friends for being in my life and making my world a beautiful and delightful place.

Bc. Ivana Michálková

Contents

1. Introduction

The innate curiosity of the Homo sapiens species has led to astonishing scientific discoveries, shedding light not only on the world around us but also within us. The human body is an extraordinarily complex machine composed of atoms connecting to molecules, forming chemical compounds, that result in the basic structural and functional unit of life - the cell. While modern optical microscopy methods have made it possible to study these structures in vitro, observing them in vivo is far more challenging. The heterogeneous nature of living tissue results in a nonuniform refractive index, leading to multiple scattering events that make it difficult to focus through thick samples and obtain high-resolution imaging quality. Despite the continuous effort to control the light propagation through a complex medium [1], most common non-invasive imaging techniques still cannot escape the trade-off between resolution and penetration depth, as portrayed in Fig. 1.1.

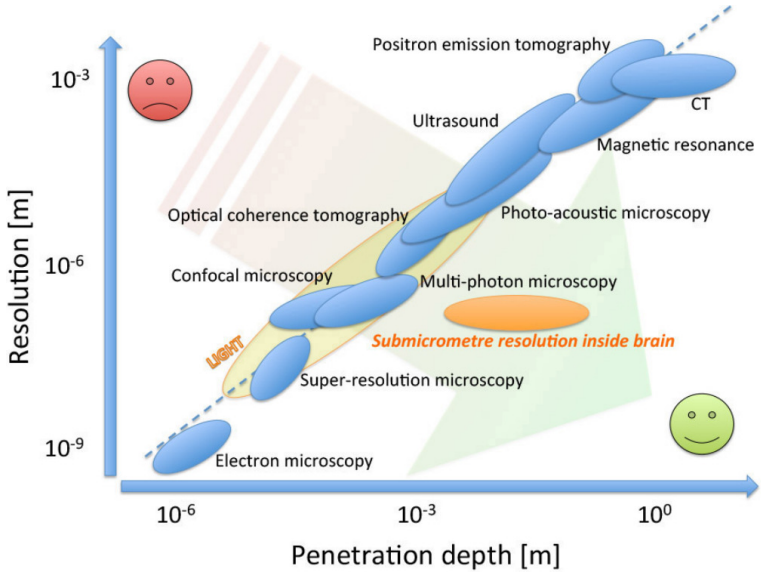

Figure 1.1: Trade-off between resolution and penetration depth for some of the most common non-invasive biomedical microscopy techniques. Figure reprinted from [2].

An alternative solution to imaging micro-structures deep inside the living tissues relies on the use of endoscopes. Surprisingly, the first idea of such a device dates back to the beginning of the 19th century [3]. Nevertheless, the design of modern endoscopes is derived from the ideas developed during the 1950s by British physicist Harold Hopkins [4, 5]. Up-to-date endoscopes are constructed either as rigid rod-lens slender structures with exceptional imaging quality or flexible fiber bundles, so-called fiberscopes.

Despite the enormous progress in endoscopy engineering, the footprint of these instruments rarely falls below 1 mm [6], causing extensive damage to the most sensitive tissues, such as the brain. Hence, the commercially available endoscopes cannot satisfy neuroscientists' burgeoning desire to study the neuron's interconnections and their communication in awake animal models.

During the first decade of this century, advancement in the field of complex media photonics [7, 8, 9] has given rise to a possible solution to the need for a new minimally invasive deep-tissue microscopy technology. The underlying idea was to use a single hair-

thin multimode fiber (MMF) as an ultra-narrow endoscopic probe [10, 11]. The significant contrast in diameter between the conventional endoscopic probes and a single MMF can be observed in Fig.1.2.

Subsequently, imaging through MMF has flourished quickly, adapting various microscopy techniques such as fluorescence [12, 13], wide-field [14], light-sheet [15], two-photon fluorescence [16, 17, 18, 19], confocal [20], Raman [21, 22] and second-harmonic generation microscopy [23] to study samples in vitro. In fact, the fluorescence imaging through MFF was not only demonstrated on the preserved samples but also applied in vivo [24, 25]. A great deal of work was also dedicated to improving the imaging speed [26, 27, 28], as well as eliminating the fiber bending influence on the imaging quality[29, 30, 31] or to the optimization of the probe ending [32, 33].

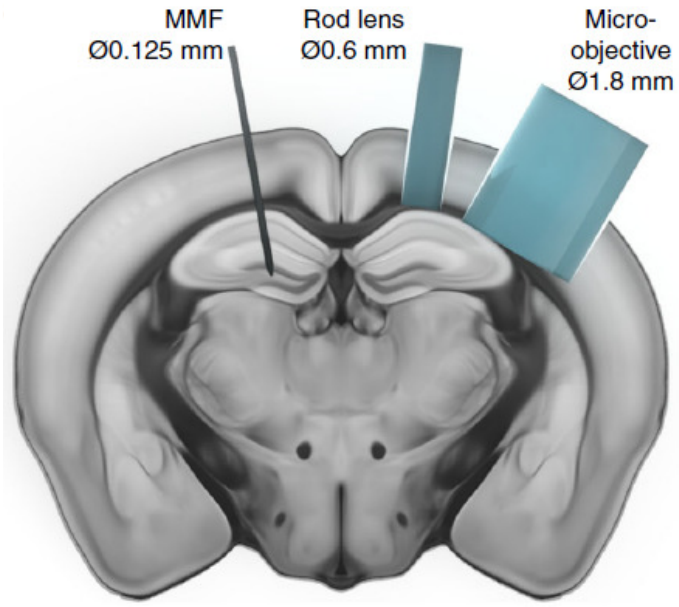

Figure 1.2: Scaled preserved comparison of standard endoscopic probes and a single multimode optical fibre when employed for microscopic imaging deep inside a mouse's brain. Figure reprinted from [24].

Moreover, in 2022 almost perfect focusing through step-index MMF was demonstrated by generating diffraction-limited foci, comprising 96 % of the power transmitted by the fiber [34]. The secret behind obtaining a diffraction-limited focus with such purity lies in the complete control over the amplitude, phase, and two orthogonal polarisation states of the light coupled into the MMF.

This thesis aims to investigate whether it is possible to produce more complex optical field distributions with comparable purity and fidelity, employing the method mentioned above [34]. For the experiment, we chose Airy beams, not only because of their direct applications in the light-sheet microscopy [35, 36] but also because, unlike the MMF, they do not follow a circular symmetry and exhibit non-diffractive quadratic propagation trajectory.

2. Basic concepts

One of this thesis's aims is to create an overview of the literature discussing the basic principles behind the method of holographic endoscopy. The root of this method lies in the ability to focus light via a multi-mode optical fiber. How this can be accomplished will be further explained in the first section (Chap. 2.1) of the thesis's theoretical part. The second section (Chap. 2.2) of the thesis's theoretical part represents a brief introduction to the optical beams and their properties, with an emphasis on the Gaussian and Airy beams.

2.1. Holographic endoscopy

Holographic endoscopy utilizes a multi-mode optical fiber (MMF) as an ultra-narrow probe for deep-tissue in vivo microscopy. However, the imaging through the MMF is not that straightforward because of a seemingly random scrambling of the light guided by the MMF. Nonetheless, during the last 15 years, several methods for overcoming this drawback have been developed and successfully implemented. The following chapters provide an overview of the basic concepts of Holographic endoscopy, starting with the fundamentals of fiber optics (Chap. 2.1.1). The next chapter 2.1.2 promptly covers the methods developed for light propagation control through a turbid media, which represent the cornerstone for techniques designed to control the propagation of light via MMF described in the following chapter 2.1.3. Lastly, the chapter 2.1.4 discusses the basic properties of two spatial light modulators, most commonly employed in holographic endoscopes.

2.1.1. Fibre optics

Optical fibers are narrow, flexible waveguides, usually of cylindrical symmetry, fabricated from silica glass. Typical fiber comprises the inner core (Fig 2.1 dark blue) and the outer cladding (Fig 2.1 light blue), with the cladding having a slightly lower refractive index than the core. Based on the ray optics approach, the light propagates through the fiber by means of total inner reflection (TIR), which takes place at the core-cladding boundary.

However, not all the incoming light can propagate through the fiber. In general, TIR can be observed only when the angle of incident light is greater than the critical angle defined for a given interface. As illustrated in Figure 2.1 a, the ray coming from air to the core becomes guided only when the refraction angle is smaller than $\overline{\theta_c}$, so that, the incident angle at the core-cladding interface would be greater than the critical angle θ_c. The rays refracting at the air-core boundary with a refraction angle higher than $\overline{\theta_c}$ can enter the fiber but will diminish after a short traveling distance because they do not undergo TIR. The incoming light angle θ_a corresponding to refraction angle $\overline{\theta_c}$, that at the core-cladding boundary correlates exactly with critical angle θ_c, is called an acceptance angle. The acceptance angle θ_a determines the size of an external ray cone, which can be guided by the fiber and is expressed as:

$$\theta_a = \sin^{-1}(NA), \tag{2.1}$$

where the NA stands for a numerical aperture that is given by:

$$NA = \sqrt{n_1^2 - n_2^2}, \tag{2.2}$$

where n_1 and n_2 correspond to the core and cladding refractive indices, respectively. In other words, the NA represents the light-gathering capacity of the fiber. Therefore, fibers with larger NA can transfer more information, as portrayed in Fig. 2.1 b.

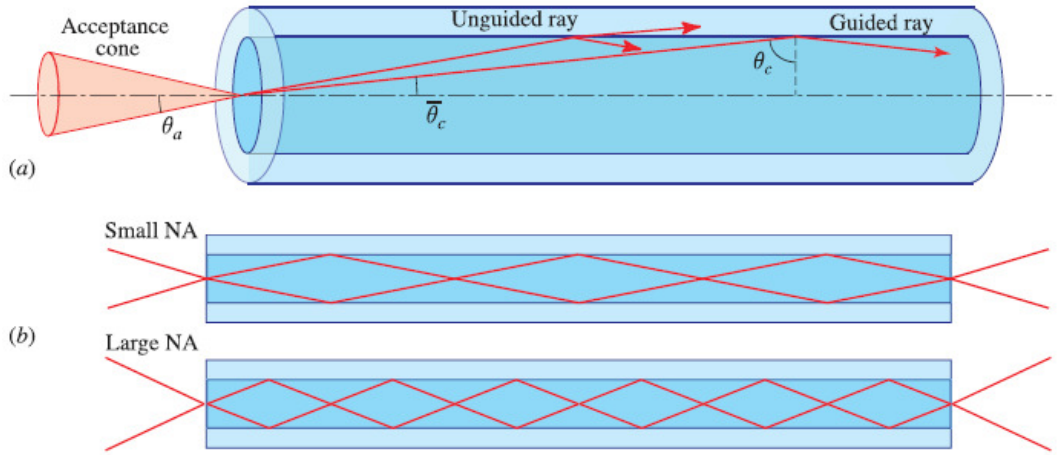

Figure 2.1: (a) The optical fibre comprises the inner core (dark blue) and the outer cladding (light blue), where the cladding has a slightly lower refractive index than the core. The acceptance angle θ_a of fibre determines the cone of rays guided through the fibre by means of TIR at the core-cladding boundary. (b) The numerical aperture $NA = sin\theta_a$ describes the light-gathering capacity of the fibre. The higher the NA, the more light is guided through the fiber. Figure reprinted from [37].

Based on the index profile, optical fibers can be classified into two distinct groups: graded-index and step-index fibres (Fig. 2.2). Graded-index (GRIN) fibers contain a core with a continuously decreasing index, which peaks at the optical axis. In contrast, the core of step-index fiber is fabricated with a constant refractive index. If the core diameter is so small that only one mode can be guided, the optical fiber is called a single-mode fiber (SMF). On the other hand, multi–mode fiber (MMF) has a larger core diameter; therefore, it can support many modes. For example, a step-index MMF (Thorlabs: FG050UGA) used for the experimental part of this thesis can guide approximately 1492 modes [38].

Generally speaking, modes of any waveguide are fields that maintain the same transverse distribution and polarization at all distances along the waveguide axis [37]. The higher amounts of modes, the more information can be transferred through the waveguide. However, each mode travels with a different group velocity, a phenomenon called modal dispersion. Furthermore, as a consequence of fiber bending and looping or inhomogeneities and impurities present within the fiber, the modes can couple with each other and exchange energy. This process is known as mode mixing. Both mechanisms, modal dispersion and mode mixing, contribute to the distortion of an incident wavefront, leading to a complex speckle pattern at the output, with very poor or no similarity to the original field distribution, as depicted in Fig. 2.3.

Due to the scrambling of the guided information, the MMFs were, for a long time, considered not suitable for microscopic imaging. Nevertheless, in recent years it has been

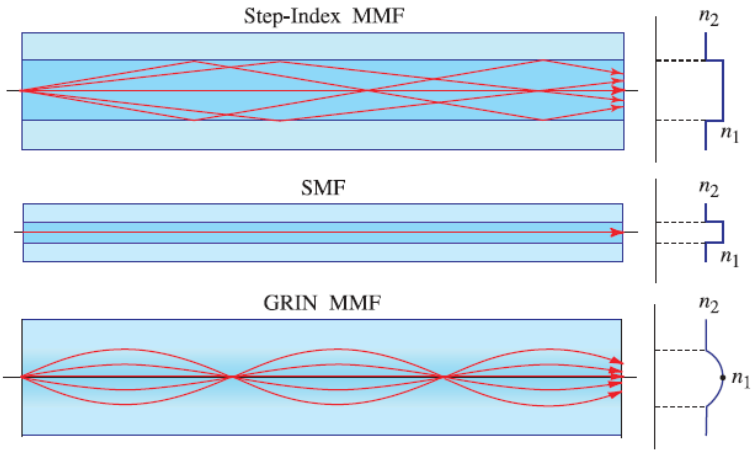

Figure 2.2: Geometry, refractive index profile, and typical rays in step-index multi-mode (MMF) fibre, a step-index single-mode fibre (SMF), and graded-index multi-mode fibre (GRIN MMF). Figure reprinted from [37].

Figure 2.3: Modal dispersion and mode mixing distort the original wavefront, resulting in a complex speckle pattern at the distal end of the MMF. Figure reprinted from [39].

shown [11, 12] that it is possible to overcome this drawback by adapting the concept of transformation matrix from the field of complex media photonics, as will be explained in the following chapters.

2.1.2. Control of light propagation through highly scattering media

As the name suggests, highly scattering media, otherwise known as complex or turbid media, scatter the propagating light in random directions, leading to a significant distortion of the incident wavefront. Therefore, the image transmission loses all the information, and the material is said to be opaque.

As biological tissue represents a typical example of an opaque material, transmitting images through a turbid medium has been one of the most desired objectives in experimental biophotonics. At the beginning of this millennium, the development of precise spatial light modulators paved the way to advance digital holography techniques, allowing the focusing of light through and into the turbid media [40]. The root of the method lies in the incident wavefront tailoring, based either on iterative algorithms [7, 41], digital phase conjugation [42, 43] or the transformation matrix concept [44, 45, 46].

Although all of these approaches have proven valid, probably the most recognized and stirring is the measurement of the medium's transformation matrix. In most cases, the complex media can be considered a discrete linear system. Hence the light propagation

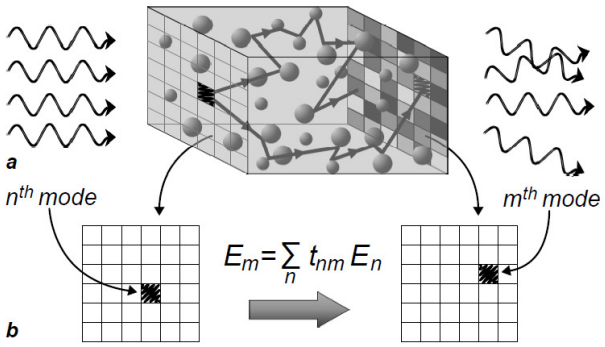

Figure 2.4: Wave propagation in complex media. (a) Wavefronts transmitted through complex media are distorted due to multiple scattering events. (b) The spatial output modes E_m are related to the input modes E_n through a transformation matrix that completely describes the optical propagation through the turbid medium. Figure reprinted from [6].

through a given media can be characterized by a matrix of complex coefficients [44]. As schematically portrayed in Fig. 2.4, this so-called transmission matrix (TM) then relates the set of orthogonal output E_m and input E_n spatial modes that, when combined, represent the transmitted and incident light, respectively. Consequently, the information about the medium stored in the TM can be utilized to determine the amplitude and phase input distribution, to obtain a demanded output field. Moreover, by employing the TM, the supposedly unpredictable speckle pattern created by image transmission through the scattering media can be reconstructed to the original data.

However, when imaging within the scattering medium, e.g., in vivo deep tissue microscopy, the access to direct observation of the output field is limited, and the TM is incomplete. Although using fluorescent particles [7, 9] or employing ultrasonic encoding [47, 48] can overcome the withstanding issue, the use of an MMF as a minimally invasive probe for accessing the deeply hidden imaging area represents a reasonable compromise.

2.1.3. Control of light propagation through MMF

Even though different phenomenons determine the randomization of light propagating through MMF, it resembles the light transmission through the complex media. Indeed, the concept of empirically measured transformation matrix [12, 14] mentioned above, alongside the digital phase conjugation technique [13, 49] and analogies of the first wavefront shaping feedback algorithms [11, 10] have been effectively adapted for beam-shaping and imaging through MMF.

When employing the TM theory for microscopy via MMF, a calibration procedure must be performed before the imaging process. During the calibration, the TM is measured as one has direct optical access to the MMF distal end. The complete description of the TM acquisition is provided in chapter 3.2. Afterward, acting as a light guiding needle, the fiber is inserted into the tissue, and the micro-scale imaging can begin. Once one has access to the TM, an arbitrary field distribution at the distal facet of the MMF can be generated by utilizing a spatial light modulator (SLM) to tailor the incident wavefront in a predefined manner. As shown in Fig. 2.5 a, producing a diffraction-limited focus at different transversal positions of the distal fiber facet enables the fluorescent imaging [50,

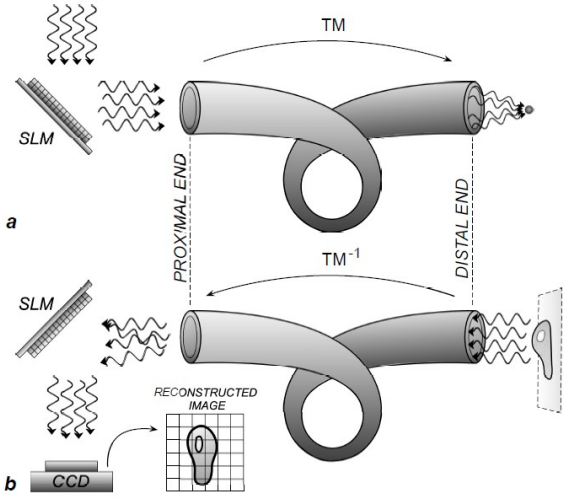

Figure 2.5: The multimode fiber as a turbid medium. (a) Focusing light through MMF. Using the information stored in the fiber's TM, one can spatially modulate the incident wavefront so that the light is tightly focused to an aberration-free diffraction-limited spot at a given working distance from the fiber's distal end. Scanning with the focus enables fluorescence microscopy or micromanipulation. (b) Wide-field imaging through MMF. Employing the TM, the optical field at a certain distance from the distal fiber facet can be restored from the speckled pattern obtained at the proximal end. This can be done either by numerical processing or by physical inversion of the TM, utilizing an SLM. Figure reprinted from [6].

12, 13] or micromanipulation [50, 12]. Moreover, scanner-free wide-field imaging can be performed when employing the TM to recover the original optical field distribution at the distal end of MMF by numerical postprocessing [14] or by physical inversion of the TM using an SLM [12], as depicted in the Fig. 2.5 b.

Clearly, the SLM plays a crucial role in beam shaping and imaging through MMF. Therefore the next chapter covers the basic concepts of digital spatial light modulation.

2.1.4. Spatial light modulators

In general, the name spatial light modulator (SLM) refers to a device capable of modulating one or more properties of light, e.g., amplitude, phase, or polarization. During the 70s-80s, novel digital light-shaping devices were introduced. This computer-controlled technology enabled the generation of any desired optical field, resulting in a considerable advancement in the field of complex media photonics [1]. For the purpose of holographic endoscopy and focusing via MMF, usually two types of digital SLM are employed. It is either a liquid crystal based modulator (LC-SLM) or a digital micromirror device (DMD), an example of a microelectromechanical system (MEMS).

Although LC-SLMs were initially developed for video projectors, they swiftly found a way to scientific applications such as holographic optical tweezers, advanced microscopic methods, holographic displays, data storage, and optical computing [51]. LC-SLM can be constructed either as a transmissive or reflective optical element. The typical configuration of a reflective LC-SLM is depicted in Fig. 2.6. The upper part is covered by glass, of which the inside layer is coated by a transparent conductive layer. In the middle,

thousands of liquid crystal molecules form the liquid crystal layer. The bottom comprises reflection pixels embedded into the silicon substrate [52]. The liquid crystal structure can be modulated by the amount of voltage applied, resulting in birefringence change, which impacts the phase of the reflected wavefront. Clearly, by utilizing the LC-SLM alone, only phase modulation is possible. However, using a computer-generated phase hologram, the modifications of the incident wavefronts in both phase and amplitude are possible [53]. Although the LC-SLMs are highly efficient with regard to power, they feature a relatively slow frame rate, which is not optimal for scanning microscopy techniques [27].

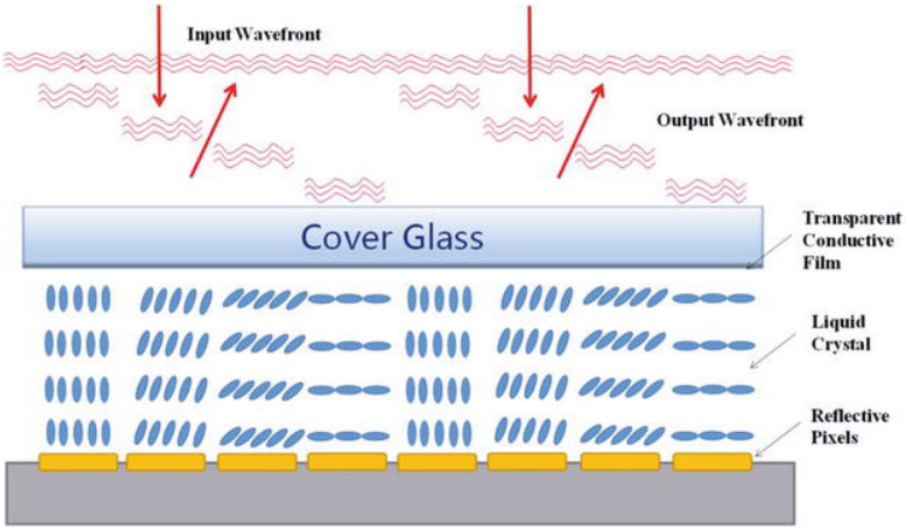

Figure 2.6: Typical structure of reflective LC-SLM. The upper part is covered by glass, of which the inside layer is coated by a transparent conductive layer. In the middle, thousands of liquid crystal molecules form the liquid crystal layer. The bottom part consists of reflection pixels embedded into the silicon substrate. The phase modulation of the reflected wavefront is enabled by the change in the tilt of liquid crystal molecules due to the amount of voltage applied to individual pixels. Figure reprinted from [52].

On the other hand, DMDs operate on a much higher frame rate, enabling faster TM acquisition and imaging based on scanning [27]. Other significant advantages of this technology are a longer lifetime and the option to work with a broader wavelength spectrum and non-polarised light [54]. As depicted in Fig. 2.7, DMD is composed of several hundred thousand tiny mirrors arranged in a rectangular array. Each mirror can be addressed in a digital manner, toggling between an on-state or an off-state, resulting in a rotation of approximately $\pm 10 - 12°$ [55].

However, as the mirrors can be switched only between two positions, the DMD, compared to LC-SLM, does not allow direct phase modulation but only binary amplitude modulation. Nevertheless, this obstacle can be overcome by employing the DMD in an off-axis regime together with the Lee hologram approach [57, 27, 58]. When working with the DMD in an off-axis regime, the DMD is illuminated under an incident angle of approximately 24° [34]. The Lee hologram method utilizes the superposition of binary amplitude gratings to form a desired complex field in the first diffraction order. As shown in Fig. 2.8 a, the distance between adjacent grooves of the grating determines the angle of the first diffraction order and, consequently, the position of the beam focused on the

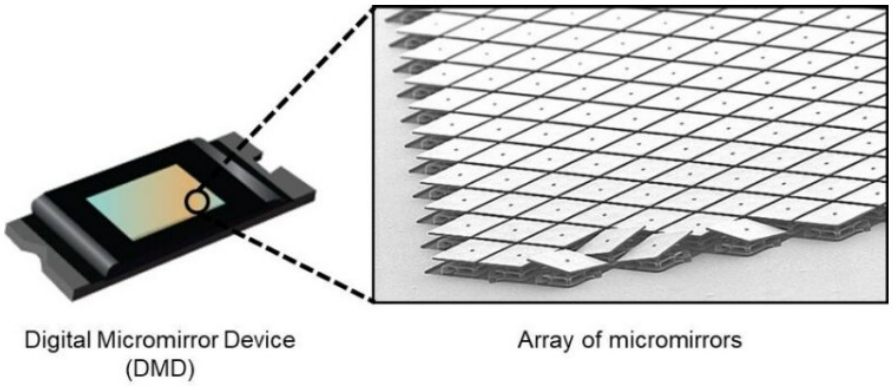

Figure 2.7: A digital micromirror device is composed of several hundred thousand tiny mirrors arranged in a rectangular array. Each tiny mirror can be set either to position on or off, resulting in the tilt of $\pm 10 - 12°$. Figure reprinted from [56].

detector. The duty of cycle defines the amount of light stirred to the first diffraction order, thus enabling the amplitude modulation (Fig. 2.8 b). Whereas implementing a lateral shift in the grating allows control over the phase of the diffracted light (Fig. 2.8 c).

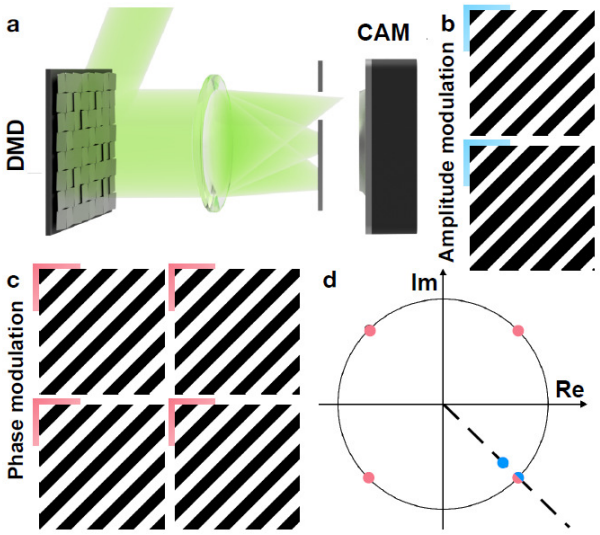

Figure 2.8: (a) Illustration of the Lee hologram method employing binary amplitude gratins for off-axis amplitude and phase modulation. (b) Amplitude is modulated by the grating's duty cycle. (c) Phase modulation is performed by the lateral shift of the grating. (d) Far-field (Fourier) plane schematically depicts the modulations acquired by the gratings presented in cases b (blue dots) and c (red dots). Figure reprinted from [51].

For the purpose of our experimental measurements, the DMD spatial light modulator was employed.

2.2. Properties of optical beams

One of this thesis's goals is to obtain an Airy beam at the tip of a multimode fiber by shaping the light produced by a laser. Laser resonators are usually constructed in such a way that the output light forms the Gaussian beam. Therefore, the following chapters promptly discuss the fundamental properties and mathematical description of beams, emphasizing the Gaussian and Airy beams.

From the scalar theory approach, light propagation can be described in the form of waves. A monochromatic wave is defined by a complex wavefunction:

$$U(\vec{r},t) = a(\vec{r})\exp[j\phi(\vec{r})]\exp(j2\pi\nu t), \tag{2.3}$$

where $a(\vec{r})$ denotes the amplitude, $\phi(\vec{r})$ signify the phase, ν stand for the frequency that when multiplied by 2π equals to the angular frequency $\omega = 2\pi\nu$. The complex wavefunction $U(\vec{r},t)$ must satisfy the wave equation:

$$\nabla^2 U(\vec{r},t) - \frac{1}{c^2}\frac{\partial^2 U(\vec{r},t)}{\partial t^2} = 0. \tag{2.4}$$

In this equation ∇^2 represent the Laplacian operator defined as:

$$\nabla^2 = \frac{\partial^2}{\partial x^2} + \frac{\partial^2}{\partial y^2} + \frac{\partial^2}{\partial z^2}. \tag{2.5}$$

The complex wavefunction can also be written as:

$$U(\vec{r},t) = U(\vec{r})\exp(j2\pi\nu t), \tag{2.6}$$

where the time-independent factor $U(\vec{r}) = a(\vec{r})\exp[j\phi(\vec{r})]$ is known as the complex amplitude. Substituting the complex wavefunction defined by Eq. 2.6 to the wave equation (Eq.2.4) yields the Helmholtz equation:

$$(\nabla^2 + k^2)U(\vec{r}) = 0, \tag{2.7}$$

where $k = (2\pi)/\lambda$ denotes the wave number in a given medium. One of the simplest solutions of the Helmholtz equation is the plane wave, whose complex amplitude is expressed as:

$$U(\vec{r}) = A\exp(-jk\vec{r}). \tag{2.8}$$

However, when the wavefront normals make a small angle with the optical axis, the wave is considered paraxial. In such cases, the complex amplitude can be modified to describe a plane wave traveling in the z-axis directions, with a complex envelope A, that becomes a slowly varying function of position. Thus we have:

$$U(\vec{r}) = A(\vec{r})\exp(-jkz). \tag{2.9}$$

As the paraxial wave (Eg. 2.9) has to be solution of the Helmholtz equation (Eq. 2.7), the complex envelope $A(\vec{r})$, must satisfy the paraxial Helmholtz equation, given by:

$$\nabla_T^2 A - j2k\frac{\partial A}{\partial z} = 0. \tag{2.10}$$

Here, $\nabla_T^2 = \frac{\partial^2}{\partial x^2} + \frac{\partial^2}{\partial y^2}$ represents the transverse Laplacian operator. Another elementary solution of the paraxial Helmholtz equation (Eq. 2.10) is the paraboloidal wave, a Fresnel approximation of the spherical wave. However, the most compelling solution of the paraxial Helmholtz equation (Eq. 2.10) is probably the Gaussian beam, which can be derived from the complex envelope of the paraboloidal wave, as will be addressed in the next chapter.

2.2.1. Gaussian beam and other selected beam forms

As mentioned in the previous chapter, the complex amplitude of the Gaussian beam can be derived from the paraboloidal wave. The paraboloidal wave is known as the Fresnel approximation of the spherical wave and represents one of the many solutions to the paraxial Helmholtz equation (Eq.2.10). The complex amplitude of the spherical wave is given by:

$$U(\vec{r}) = \frac{A_0}{r} \exp(-jkr), \tag{2.11}$$

where r is the distance from the origin, $k = (2\pi)/\lambda$ symbolize the wavenumber and A_0 is a constant.

Nonetheless, if we were to examine the wavefronts of the spherical wave far from the origin, but still sufficiently close to the optical axis (z) so that $\sqrt{x^2 + y^2} \ll z$ as depicted in Fig.2.9, employing the first two terms of the Taylor-series expansion, we would obtain a complex amplitude of the paraboloidal wave, which can be expressed as:

$$U(\vec{r}) \approx \frac{A_0}{z} \exp(-jkz) \exp\left(-jk\frac{x^2 + y^2}{2z}\right), \tag{2.12}$$

and the complex envelope of the paraboloidal wave is given by:

$$A(\vec{r}) = \frac{A_1}{z} \exp\left(-jk\frac{x^2 + y^2}{2z}\right). \tag{2.13}$$

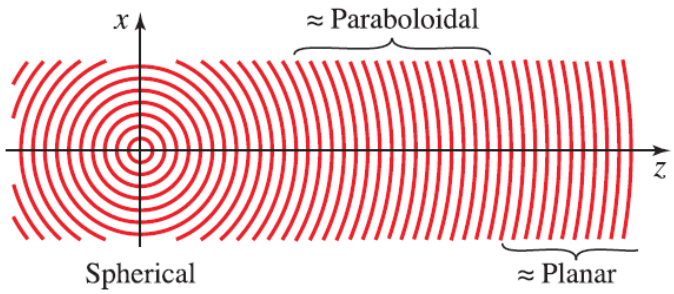

Figure 2.9: When $\sqrt{x^2 + y^2} \ll z$, the spherical wave can be approximated by the paraboloidal wave, otherwise known as the Fresnel approximation of the spherical wave. At a distance $z \to \infty$, the spherical wave can be considered planar. Figure reprinted from [37].

The Gaussian beam's complex envelope is a shifted version of the complex envelope derived for the paraboloidal wave (Eq. 2.13). As a result, the complex envelope of a

Gaussian beam can be obtained by replacing the term z in the Eq. 2.13 with a so-called q-parameter q(z) so that:

$$A(\vec{r}) = \frac{A_1}{q(z)} \exp\left[-jk\frac{x^2+y^2}{2q(z)}\right], \tag{2.14}$$

where the q-parameter $q(z) = z + jz_0$, and z_0 must be real. The imaginary part jz_0 signifies the shift in the z coordinate, and the term z_0 is called the Rayleigh range.

To derive the complex amplitude $U(\vec{r})$ of the Gaussian beam, we need to separate the amplitude and phase of the complex envelope $A(\vec{r})$. This can be done by defining two new functions $R(z)$ and $W(z)$, that relate to the q-parameter by:

$$\frac{1}{q(z)} = \frac{1}{R(z)} - j\frac{\lambda}{\pi W^2(z)}. \tag{2.15}$$

The function $R(z)$ represents the beam's wavefront radius curvature, and $W(z)$ is the beam's half-width at a given position z.

Finally, by substituting the Eq. 2.15 into Eq. 2.14 and utilizing the relation for the complex amplitude of the paraxial wave (Eq. 2.9), we can obtain the complex amplitude of the Gaussian beam:

$$U(\vec{r}) = \frac{A_1}{jz_0}\frac{W_0}{W(z)} \exp\left[-\frac{x^2+y^2}{W^2(z)}\right] \exp\left[-jkz - jk\frac{x^2+y^2}{2R(z)} + j\zeta(z)\right], \tag{2.16}$$

where $\zeta = \tan^{(-1)}\left[\frac{z}{z_0}\right]$ and term W_0 denotes the beam's radius at position $z = 0$. This position is known as the beam's waist, and it is the point of a minimal width $W(z) = W_0$ as depicted in Fig. 2.10 a.

Nonetheless, common detectors are equipped to measure the intensity, which can be calculated as the squared magnitude of the complex amplitude the $I(\vec{r}) = |U(\vec{r})|^2$. With this in mind, the intensity of the Gaussian beam can be defined as:

$$I(\rho, z) = I_0\left[\frac{W_0}{W(z)}\right] \exp\left[\frac{-2\rho^2}{W^2(z)}\right], \tag{2.17}$$

where $\rho = \sqrt{x^2+y^2}$ represents the radial coordinate. I_0 is a constant representing the maximum intensity of the beam. The term $[W_0/W(z)]$ represents the beam width ratio, which accounts for the variation in beam width as a function of the propagation distance z. The exponential term $\exp[-2\rho^2/W^2(z)]$ describes the spatial intensity distribution of the Gaussian beam, which exhibits a bell-shaped profile centered around the beam axis. The intensity distributions of the Gaussian beam at different propagation distances are illustrated in Fig. 2.10 b, c, d.

However, in addition to the Gaussian beam, there exist other beam-like solutions of the paraxial Helmholtz equation (Eq. 2.10). One such example is the family of Hermite-Gaussian beams. These beams feature a non-Gaussian intensity distribution, but their wavefronts are equivalent to those of the Gaussian beam. These beams coexist with the Gaussian beam inside a laser resonator cavity and are referred to as the modes of the resonator, with the Gaussian beam being the fundamental mode [37]. The intensity distribution of selected Hermite-Gaussian beams is illustrated in Fig. 2.11 a.

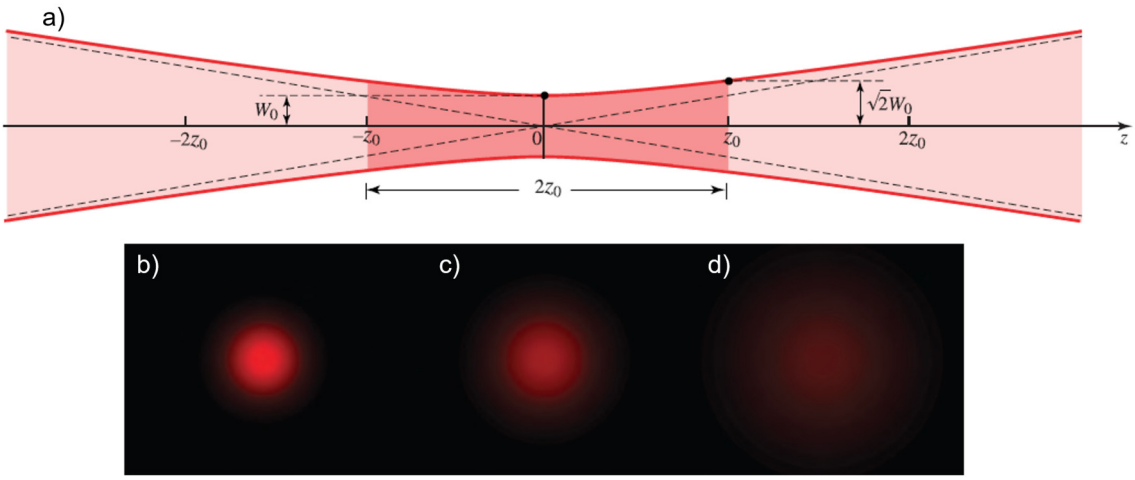

Figure 2.10: Gaussian beam. a) shows the width of the Gaussian beam throughout the propagation in the z-axis direction. At $z = 0$, the beam half-width $W(z)$ reaches its minimum W_0. This place is known as the beam waist. At $z = z_0$ the half-width $W(z) = \sqrt{2W_0}$. The distance z_0 is called the Rayleigh range, and the distance $2z_0$ (dark red) is known as the confocal parameter. Figures b),c) and d) depicts the intensity of the beam at distances $z = 0$, $z = z_0$, and $z = 2z_0$, respectively. Figure reprinted and modified from [37].

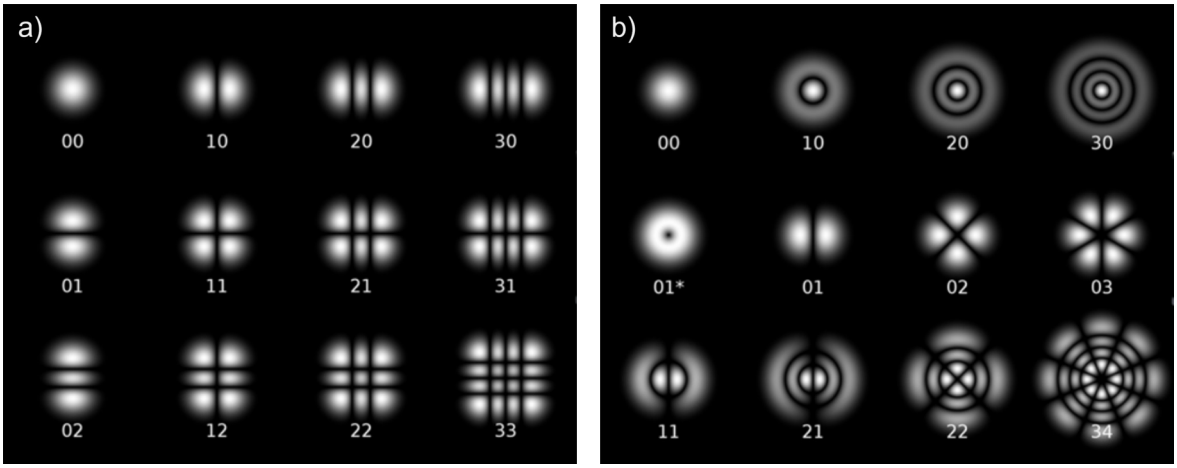

Figure 2.11: Transverse intensity distribution of selected beam-like solutions to the paraxial Helmholtz equation. a) Hermite-Gaussian beams are the modes of the laser resonator, with the Gaussian beam (00) being the fundamental mode. b) Laugerre-Gaussian beams form the set of solutions to the paraxial Helmholtz equation solved in cylindrical coordinates. Of particular importance is the Vortex beam (01*), finding its applications across numerous fields. Figure reprinted and modified from [59, 60].

By solving the paraxial Helmholtz equation in cylindrical coordinates, another set of solutions known as the Laugerre-Gaussian beams can be obtained. The intensity distribution of selected Laugerre-Gaussian beams can be seen in Fig. 2.11 b.

Among the Laguerre-Gaussian family, a particularly interesting member is the vortex beam denoted as 01* in Figure 2.11b. This beam has found various applications across

different fields, ranging from optical manipulation, optical communication, and quantum information processing to imaging and microscopy [61].

Another compelling class of beams represent the non-diffracting beams, such as Bessel or Airy beams. Bessel beams, characterized by the central bright spot surrounded by concentric rings, are widely used in optical trapping and manipulation, laser material processing, optical coherence tomography, optical microscopy, and optical communication [62].

Vortex, Bessel, Airy, or other unique beam forms can be tailored from the Gaussian beam either by using optical components such as axicon and annular aperture or by employing digital SLM. In this thesis, such light-shaping was used to create an Airy beam, of which properties, applications, and generation will be discussed in the next chapter.

2.2.2. Airy beam and its applications

The Airy beam possesses fascinating properties that almost seem like a magic trick. When propagating through a free space, the light in the form of an Airy beam exhibits a curved trajectory without the need for any external force. It is caused by its self-acceleration character, that is, the ability to accelerate without any external energy. Furthermore, the Airy beam belongs to the class of non-diffracting beams, which means that its transverse intensity distribution remains unchanged during propagation. Lastly, the Airy beam features a self-healing property that refers to an ability of a beam obstructed by an opaque object to reconstruct itself after traveling a certain distance.

The concept of freely-accelerating wave packets was first revealed by Berry and Balazs in 1979 [63]. The idea originated from the field of quantum mechanics, leading to a mathematical prediction that a free-particle nonlinear Schrödinger equation can manifest a shape-preserving accelerating Airy packet solution. Surprisingly, the work remained relatively unnoticed for almost 30 years, until 2007, when the finite Airy beam was predicted and experimentally realized [64, 65].

Thanks to its unique characteristics, the Airy beam has been proposed and highly touted for many applications, including optical trapping and manipulation [66, 67], particle clearing [68], regulation of plasmon channel [69], laser material processing [70], optical communications [71] and spatiotemporal bullets [72]. As mentioned in the previous chapter (Chap. 2.1.2), the light propagating through the living tissue undergoes multiple scattering events, which does not meet optimal conditions for in vivo imaging. However, the non-diffractive and self-healing properties of the Airy beam make it a great solution to this problem. By utilizing this beam in the light-sheet fluorescence microscopy, the field-of-view [35, 73, 36] and the depth of penetration can increase extensively [74]. An improvement in label-free imaging through a turbid media was also demonstrated [75], while the advantage of the parabolic trajectory associated with the self-acceleration has been utilized to locate the molecules in 3D super-resolution microscopy along the axial direction [76]. Moreover, it has been shown that employing an Airy beam in optical coherence tomography can significantly improve the depth of field limit [77].

From the mathematical point of view, an Airy beam represents another solution of the paraxial Helmholtz equation (Eq.2.10). This equation is mathematically equivalent to the Schrödinger equation of a free quantum particle in two dimensions; hence the connection

to quantum mechanics in work done by Balazs and Berry in 1979 [63]. According to them, the complex envelope of a one-dimensional Airy solution has a form of:

$$A(x,z) = \mathrm{Ai}\left[\frac{x}{W_0} - \left(\frac{z}{4z_0}\right)^2\right] \exp\left[\frac{jx}{W_0}\frac{z}{4z_0} - \frac{j}{12}\left(\frac{z}{2z_0}\right)^3\right], \tag{2.18}$$

where Ai(x) denotes the Airy function. The parameters W_0 and z_0 represent the transverse and axial scaling factors, respectively. Similarly to the Gaussian beam, the parameters are related to each other by $W_0^2 = \lambda z_0/\pi$.

The intensity derived from Eq. 2.18, can be expressed as:

$$I(x,z) = \mathrm{Ai}^2\left[\frac{x}{W_0} - \left(\frac{z}{4z_0}\right)^2\right]^2. \tag{2.19}$$

At the origin (z=0), the intensity obtains a form of $I(x,0) = \mathrm{Ai}^2(x/W_0)^2$, and remains invariant during propagation. The second term $(z/4z_o)^2$ characterizes the ballistic trajectory caused by the transverse acceleration while traveling in the z-direction [65, 78].

Providing the ideal conditions, the Airy beam would have infinite energy, and consequently, it would maintain its transverse acceleration and diffraction-free propagation regardless of its propagation distance. The propagation of such beams is depicted in Figure 2.12 a. Although the infinite energy beams are impossible to create experimentally, it is achievable to generate a truncated Airy beam [64, 78], of which trajectory can be seen in Figure 2.12 b.

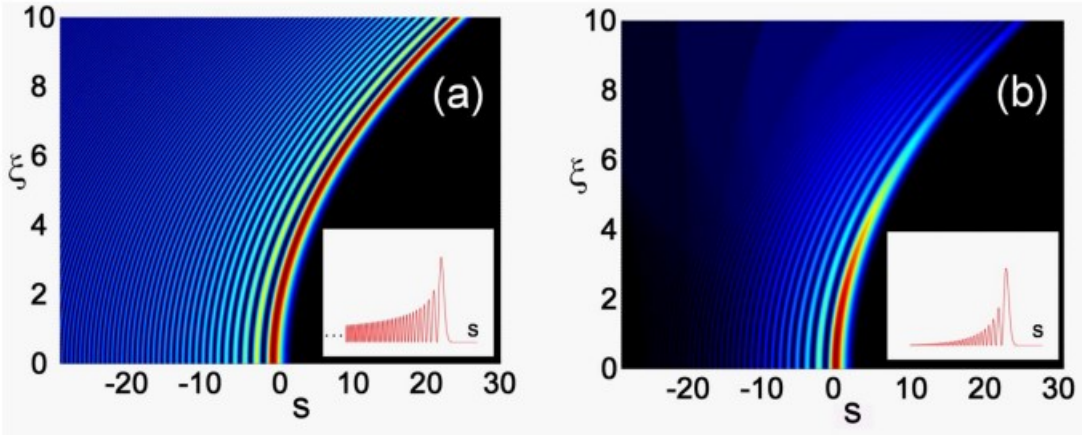

Figure 2.12: Propagation of 1D infinite (a) and truncated (b) Airy beam, where $s = x/W_0$ and $\xi = z/2z_0$ represent dimensionless scaling factors. The figures in the lower right corner show the beam's intensity profile at $\xi = 0$. Figure reprinted from [65].

The Airy beam truncation can be mathematically expressed by :

$$A(x,0) = \mathrm{Ai}\left(\frac{x}{W_0}\right) \exp\left(\alpha\frac{x}{W_0}\right), \tag{2.20}$$

where the $\alpha > 0$ represents an attenuation factor. The finite Airy beam's complex envelope can be obtained by solving the paraxial Helmholtz equation (Eq. 2.10) with regards

to the initial condition (Eq. 2.20) [64, 78]. From this complex envelope, the intensity of the finite Airy beam can be expressed as:

$$I(x,z) = \mathrm{Ai}^2\left[\frac{x}{W_0} - \left(\frac{z}{4z_0}\right)^2\right]^2 \exp\left[\frac{\alpha x}{W_0} - \frac{\alpha}{2}\left(\frac{z}{2z_0}\right)^2\right]^2. \tag{2.21}$$

As it was demonstrated in [64, 78], the truncated Airy beam possesses a quasi-diffraction-free character and endures the property of free acceleration related to the argument of an Airy function that appears in Eq. 2.21.

In our experiments, we generate two-dimensional Airy beams [65, 78]. The intensity at the origin of such a beam is given by:

$$I(x,y,0) = \mathrm{Ai}^2\left[\frac{x}{W_0}\right]^2 \mathrm{Ai}^2\left[\frac{y}{W_0}\right]^2 \exp\left[\frac{\alpha x}{W_0}\right]^2 \exp\left[\frac{\alpha y}{W_0}\right]^2. \tag{2.22}$$

The Fourier transform of an Airy beam solution provides a Gaussian beam, described in Chap. 2.2.1, superimposed with a cubic phase mask. Thus the Airy beam can be synthesized from a Gaussian beam by incorporating a cubic phase mask to its Fourier spectrum [78]. The cubic phase mask can be produced using a spatial light modulator mentioned in Chap. 2.1.4.

3. Methods

The following chapters provide a theoretical description of the methods utilized during the experimental work presented in this thesis. Chapter 3.1 provides a concise overview of the optical setup that was employed in the experiments conducted for this master's thesis. It describes the key components and their functions within the experimental setup. Chapter 3.2 provides a detailed explanation of the calibration procedure, that was performed prior to the actual measurements, in order to obtain the TM of the multimode fibre. The chapters 3.3 and 3.4, delve into two distinct methods used for the generation of Airy beams. Each chapter provides a detailed description of the respective method, including the underlying principles and mathematical formulations. The last chapter of this section (Chap.3.5) explains an approach utilized to modify the propagation characteristics of an Airy beam. This chapter discusses a particular technique that was used to alter the behavior of the Airy beam during propagation, namely its propagation range, the trajectory starting point, and the position of the intensity peak during propagation.

3.1. Optical setup

For the experimental part of this thesis, an optical setup described in [34] was employed. As illustrated in Fig. 3.1, the system is composed of an illumination path, a calibration module, and a wavefront correction (WFC) module.

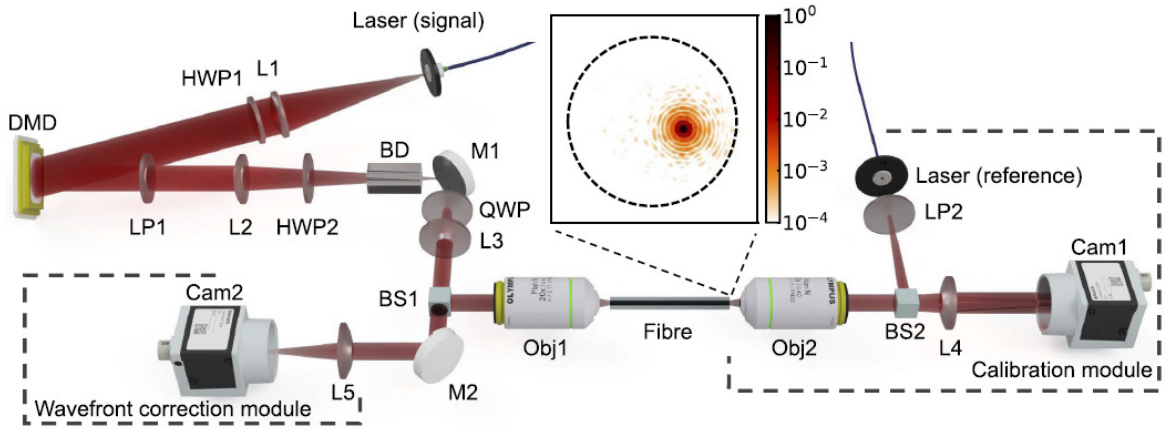

Figure 3.1: Scheme of the experimental setup. During calibration, circularly polarised light, whose aberrations were previously corrected by the wavefront correction module, is coupled into the MMF. At the calibration module, the signal coming from the MMF interferes with the reference, and the camera measures the interference pattern. Legend: L, lens; HWP, half-wave plate; DMD, digital micromirror device; LP, linear polariser; BD, beam displacer; M, mirror; Obj, objective; QWP, quarter-wave plate; BS, beamsplitter cube; Cam, camera. Figure reprinted from [34].

A fiber-coupled diode laser operating at the wavelength 633 nm is divided into signal and reference arm, utilizing a 99/1 optical fibre coupler. A polarisation-maintaining (PM) fiber-controlled electronic variable optical attenuators are employed to regulate the optical

power flowing into both signal and reference PM fibres. The lens L1 collimates the linearly polarised signal beam from the PM fiber to illuminate the DMD.

As explained in the Chapter 2.1.4, using DMD in an off-axis regime together with the binary-amplitude gratings, based on the Lee Hologram method [57], enables the control over both amplitude and phase of the reflected light. Thus the incident beam's path is aligned to make an angle of 24° with respect to the DMD.

The half-wave plate (HWP1) rotates the linear polarization of the signal to match the preferential direction (s or p) of the DMD mirrors because, if not appropriately aligned, the diffracted beam's polarization may become elliptical. Furthermore, a linear polarizer (LP1) is placed after the DMD to secure the linear polarization state of the diffracted light completely.

It was shown [79] that the stability of a DMD-based wavefront shaping system can be significantly extended by controlling and stabilizing the DMD's temperature. Thus, the temperature stabilization technique is also utilized in this experimental setup.

The lenses L2 and L3 form a telescope that demagnifies the beam, and the HWP2 rotates the beam's polarization at 45° concerning the principal axes of the beam displacer (BD). Upon passing through BD, the light polarized this way will split into two components, the ordinary and extraordinary rays. Moreover, the BD can merge two beams if they are separated by a distance required by the particular BD, in this case, 2.7 mm. This separation can be acquired by the correct design of two binary-amplitude gratings displayed at the DMD. As a result, two colinear beams with mutually orthogonal polarisation states are generated at the BD distal end, as portrayed in Fig. 3.2.

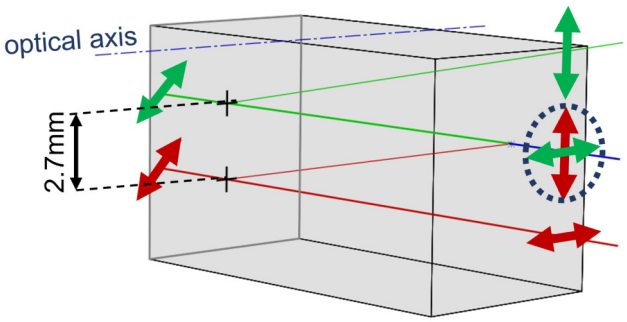

Figure 3.2: Scheme of the light passing through the beam displacer (BD). Two linearly polarized beams, with the polarization aligned at 45° concerning the optical axis of BD and separated by the distance of 2.7 mm, will, upon passing through the BD, merge into two collinear beams with mutually orthogonal polarization state (marked by the dashed circle).

After the BD, the quarter-wave plate (QWP) converts the two orthogonal linear polarizations into right and left circularly polarized beams, as the step-index multimode fibre maintains the circular polarization better than the linear [29].

A beam splitter cube (BS1) sends 90 % of the beam to the objective (Obj1) that focuses the beam onto the MMF's core, and 10 % of the beam is focussed by the lens (L5) onto the CMOS camera (Cam2). The lens (L5) and camera (cam2) form the WFC module. The WFC module allows for the determination of the correction phase mask needed for the DMD. This correction compensates for the aberrations introduced by the

curvature of the DMD, ensuring proper beam focusing onto the proximal end of the MMF during calibration.

The optical system comprising L1, L2, and Obj1 demagnifies the DMD holograms to suit the MMF's numerical aperture (NA). Our experiment employed a step-index MMF of length 11 cm with a core diameter of 50 µm, an outer diameter of 125 µm, and 0.22 NA.

The second objective (Obj2), together with the lens (L4), projects the light coming from the distal end of the MMF onto the camera (Cam1). For the experiments presented in chapters 4.1 and 4.2, the 40x objective was employed, and for the data measurement shown in chapter 4.3, a 20x objective was used. The lens L4 also collimates the reference beam, of which linear polarization state is ensured by the PM fiber-controlled electronic variable optical attenuator and linear polarizer (LP2). Moreover, the reference beam's polarization and the LP2 match one of the principal polarization axes of the 50/50 beamsplitter cube (BS2) to secure a clear polarization state at Cam1. This configuration allows interference between the linearly-polarized reference and the signal from the MMF in both left and right circular polarization states.

3.2. Calibration

In order to generate an arbitrary optical field at the distal end of MMF, first, the process of acquiring the TM must be performed. This process is usually called the calibration.

In our experiment, the calibration is done by projecting an aberration-free diffraction-limited focus at a specific position across the proximal end of MMF. The light coming out of the MMF interferes with the external reference, and the camera detects the interference pattern. Moreover, to obtain phase information, phase step interferometry is employed. After the first diffraction-limited focus is measured, the patterns displayed on the DMD are changed to create a new focus at different positions at the MMF proximal facet, and the entire process is repeated. Once the proximal end of the MMF is scanned across the predefined grid, as shown in Fig. 3.3 a, the calibration is completed.

For the calibration performed during our experiments, a grid of 61 input points was employed, and the outputs were measured by utilizing the grid of 272 by 272 camera pixels. Hence the TM matrix contained 272^2 rows (outputs) and 61^2 columns (inputs), representing the transformation between the input patterns sent to the fiber and the resulting output patterns at the distal end of the MMF. For the phase measurement, four-phase steps shifted by $\pi/4$ were used.

3.3. Fourier domain synthesis

As mentioned in Chap. 2.2.2, an Airy beam can be generated from a Gaussian beam using a cubic phase mask. The Fourier domain synthesis is based on a similar principle. Here, the cubic phase mask is integrated into the TM, and from this altered TM, one can generate an input pattern projected on the DMD that will, upon propagation through MMF, transform into an Airy beam.

The cubic phase mask needed to create Airy beams is generally given by:

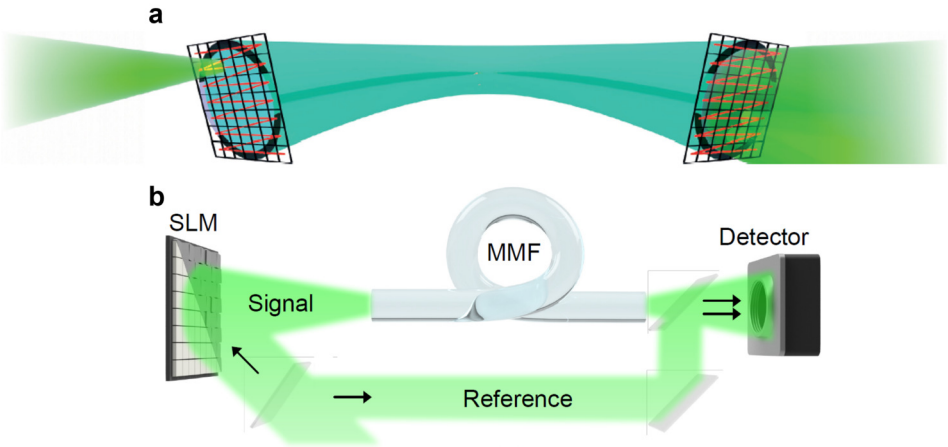

Figure 3.3: (a) During the calibration, the proximal end of the fiber is scanned by a diffraction-limited focus across a predefined grid, as depicted by the red line. (b) The light coming out of the MMF interferes with the reference, and by utilizing the phase step interferometry, the complex TM is obtained. Figure reprinted and modified from [29, 80].

$$Mask = \exp\left\{ i.b. \left[\left(\frac{X}{NA} \right)^3 + \left(\frac{Y}{NA} \right)^3 \right] \right\}, \tag{3.1}$$

where b is a chosen parameter that determines the strength of the mask. X and Y represent a grid with the sampling corresponding to TM's outputs, which also corresponds to the number of camera pixels used during the calibration procedure. Finally, NA stands for a numerical aperture of the fiber output, which was, in this case, obtained through a sum projection of the far field.

However, when employing this mask, the main lobe of propagating Airy beam was moving diagonally concerning the x and y coordinates. To achieve a movement of the main lobe only along a horizontal axis, we applied a coordinate change to rotate the Cartesian coordinate system by 45°, which simplified later analysis. An example of such a mask with the strength of $b = 5$ is captured in Fig. 3.4 a. Moreover, we applied a super-Gaussian aperture to the amplitude of the mask to avoid possible effects of hard aperturing. The super-Gaussian aperture is given by:

$$Aperture = \exp\left[- \left(\frac{\theta}{NA} \right)^{(2.N)} \right], \tag{3.2}$$

where θ represents the angular projection of the output angle obtained through a sum projection. NA signifies the numerical aperture of the MMF, and N is an integer that dictates the strength of the Gaussian aperture. The intensity distribution of the super-Gaussian aperture with a strength of N = 3 is displayed in Fig. 3.4 b. After the alterations mentioned above, the mask was modified as:

$$Mask = \exp\left\{ i.b. \left[\left(\frac{X - Y}{\sqrt{2}.NA} \right)^3 + \left(\frac{X + Y}{\sqrt{2}.NA} \right)^3 \right] \right\} .Aperture \tag{3.3}$$

Incorporating the cubic phase mask into TM can be done either by performing a convolution in a real domain or multiplication in a Fourier domain. With our equipment, the

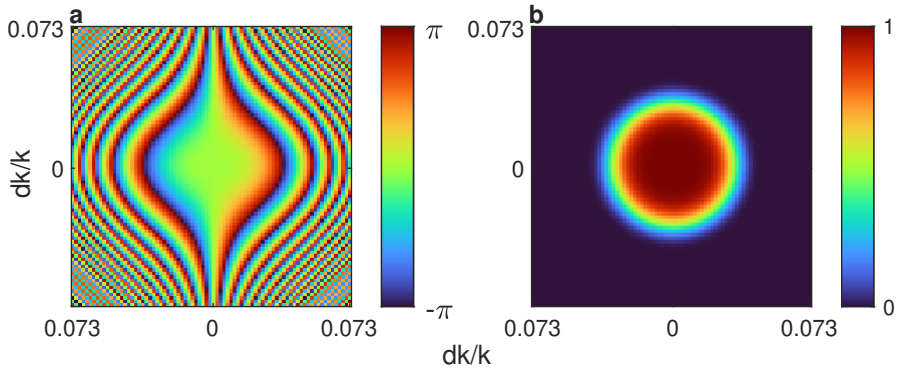

Figure 3.4: (a) Rotated cubic phase mask, used for generating an Airy beam via the Fourier domain approach. The strength of the mask corresponds to $b = 5$. (b) The intensity of the super-Gaussian aperture, with parameter $N = 3$, was applied to the cubic phase mask to avoid possible effects of hard aperturing.

second way was less time-consuming and much more straightforward, so after reshaping every output of the TM to the original size (272 by 272 pixels), a two-dimensional Fourier transform of the outputs, followed by multiplication with the phase mask, was performed (Fig 3.5). After the inverse two-dimensional Fourier transform, an altered transmission matrix was obtained. Additionally, to emulate the real conditions, the modified TM was cut by a circular mask representing the fibre's core (Fig. 3.5 d). This altered TM contains the information needed for creating a beam at any desired position at the calibration plane. This information was computationally converted into holograms projected on DMD to generate an Airy beam (Fig. 3.5 e).

3.4. Direct field synthesis

The direct field approach to obtaining an Airy beam at the end of MMF is based on computational generation of the desired output field (E_{out}), from which, by utilizing the TM theory, one can directly generate the input field (E_{in}), that is converted to a DMD input pattern necessary to send into the MMF.

As depicted in Fig. 3.6, to create 2D matrix containing the desired output field (E_{out}) (Fig. 3.6 h), we first generated two 1D finite Airy beams E(X) (Fig. 3.6 a) and E(Y) (Fig. 3.6 b), that were multiplied to get a finite 2D Airy beam E(X,Y), which can be expressed as :

$$E(X,Y) = \mathrm{Ai}\left[\frac{-(X-X_0)}{\sqrt[3]{3b}}.k.NA\right].\mathrm{Ai}\left[\frac{-(Y-Y_0)}{\sqrt[3]{3b}}.k.NA\right], \tag{3.4}$$

where Ai implies an Airy function of the first kind. X and Y represent a grid with the sampling corresponding to TM's outputs. X_0 and Y_0 determine a position of an Airy beam, concerning x and y coordinates of the calibration plane. b is a parameter designated in a way that it would relate to the strength of the cubic phase mask used to generate an Airy beam utilizing the Fourier domain approach (Chap. 3.3). $k = (2\pi)/\lambda$ is a wave number, where λ stands for the wavelength in given medium. NA signifies the numerical aperture of the multimode fiber.

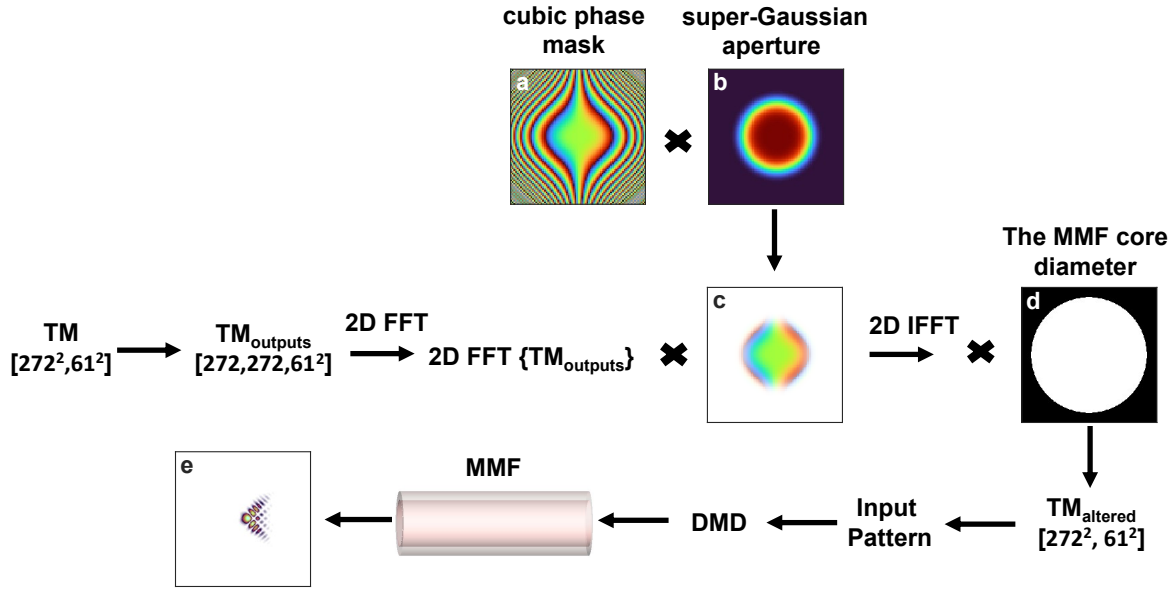

Figure 3.5: Scheme describing the Fourier domain synthesis. The product of multiplication (c) between cubic phase mask (a) and a super-Gaussian aperture (b) was in a Fourier domain incorporated into each TM's output and in a real domain cropped by a circular mask representing the MMF's core (d). From this altered TM we generated an input pattern that was projected on the DMD and, after propagation through MMF, transformed into an Airy beam (e).

However, when employing this equation, the main lobe of propagating Airy beam was again moving diagonally with respect to the x and y coordinates. Thus, we applied the same coordinate change as in Chap. 3.3, to achieve a movement of the main lobe only along a horizontal axis. After the rotation, the finite 2D Airy beam (Fig. 3.6 c) was given by:

$$E(X,Y) = \mathrm{Ai}\left[\frac{-(X-X_0)-(Y-Y_0)}{\sqrt{2}.\sqrt[3]{3b}}.k.NA\right].\mathrm{Ai}\left[\frac{-(X-X_0)+(Y-Y_0)}{\sqrt{2}.\sqrt[3]{3b}}.k.NA\right]. \tag{3.5}$$

Moreover, to emulate the real conditions, the beam was, in a Fourier domain, cropped by the fiber's numerical aperture (Fig. 3.6 d, e). Furthermore, after performing an inverse Fourier transform, the beam was cut by a circular mask representing the fiber's core (Fig. 3.6 f, g, h).

Once one has access to the information stored in TM, the field distribution that needs to be sent to the MMF (E_{in}) in order to obtain the desired field distribution at the distal end of the MMF (E_{out}), can be calculated by direct matrix multiplication in the form of:

$$E_{in} = TM^T.E_{out}, \tag{3.6}$$

where TM^T represents the transpose of the TM, used here as an approximation of the TM's inverse, and E_{out} stands for the 1D array containing the desired output field, obtained by reshaping the 2D matrix ($E_{out}(X,Y)$). Afterward, the input field E_{in} was converted into an input pattern that was projected on the DMD and, after propagation through the MMF, transformed into an Airy beam (Fig. 3.6 i).

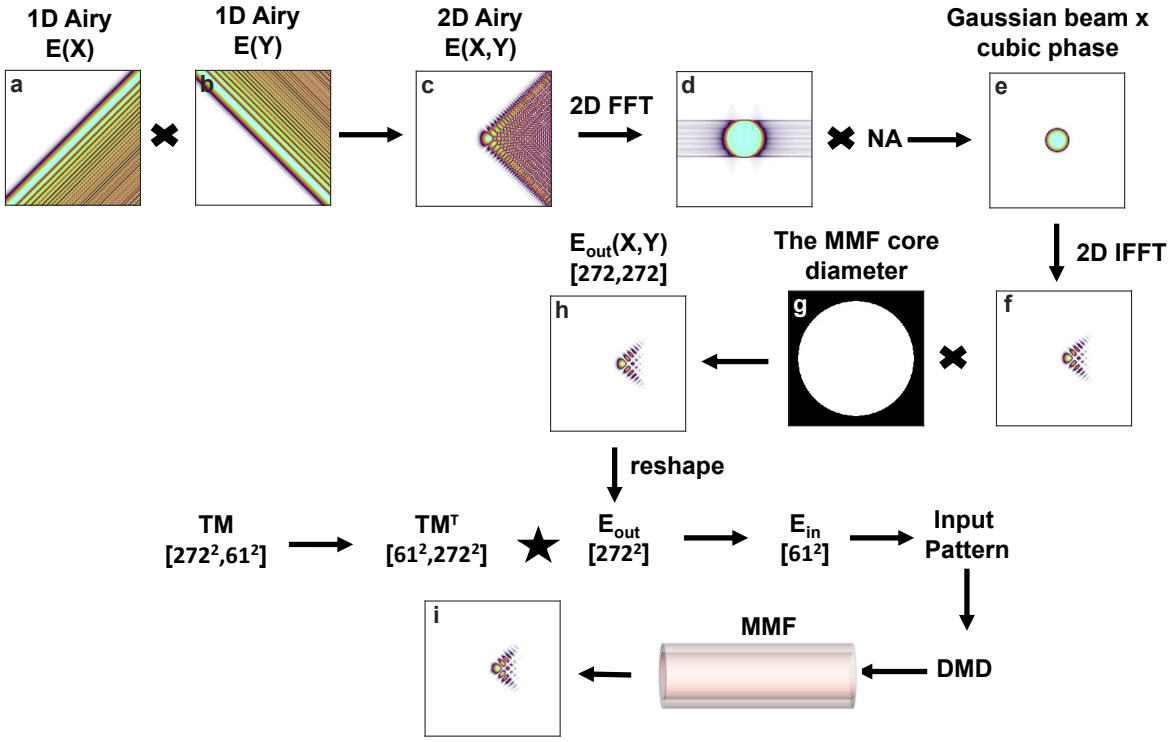

Figure 3.6: Scheme describing the direct field synthesis. To create an Airy beam via MMF, we first computationally generated two 1D finite Airy beams (a,b), of which a multiplication product is a 2D finite Airy beam (c). To emulate real conditions, this beam was in a Fourier domain (d) cropped by the MMF's numerical aperture (NA) and in the real domain cut by a circular mask representing the MMF's core (f,d). The resulting field distribution (h) was reshaped to a 1D matrix E_{out}, that after matrix multiplication (the black star) with a TM transpose (TM^T) generated an input field E_{in}. Afterward, the input field was converted into an input pattern that was projected on the DMD and, after propagation through MMF, transformed into an Airy beam (i).

3.5. Control of the ballistic motion

The characteristics of an Airy beam, such as the propagation start, trajectory range, and intensity peak position, can be further modulated as described in [78]. Using our setup, this can be done by employing both the direct field and the Fourier domain synthesis. However, utilizing the direct field synthesis, one has to calculate the exact formula describing the modified Airy beam. Whereas when exploiting the Fourier domain approach, one only needs to adjust the position of the cubic phase mask and the super-Gaussian aperture with respect to the optical axis. Therefore the Fourier domain synthesis can be accounted as a more flexible and faster method to control the propagation and position of the intensity peak of an Airy beam.

To showcase this flexibility, we displaced the super-Gaussian aperture or the cubic phase mask of strength $b = 10$ in a plane transversal to the optical axis. As portrayed in Fig. 3.7 a, to generate the conventional Airy beam described in previous chapters, the phase mask and the super-Gaussian aperture, represented by a black circle, need to be coaxially aligned. In order to create the modified Airy beams, we have tried four different misalignments. Firstly, we displaced only the phase mask along the horizontal axis (Fig.

3.7 b). Secondly, only the super-Gaussian aperture was shifted along the horizontal axis (Fig. 3.7 c). Thirdly, we moved both the phase mask and the super-Gaussian aperture in opposite directions along the horizontal axis (Fig. 3.7 d). And lastly, the phase mask and super-Gaussian aperture were misaligned together along the horizontal axis (Fig. 3.7 e)

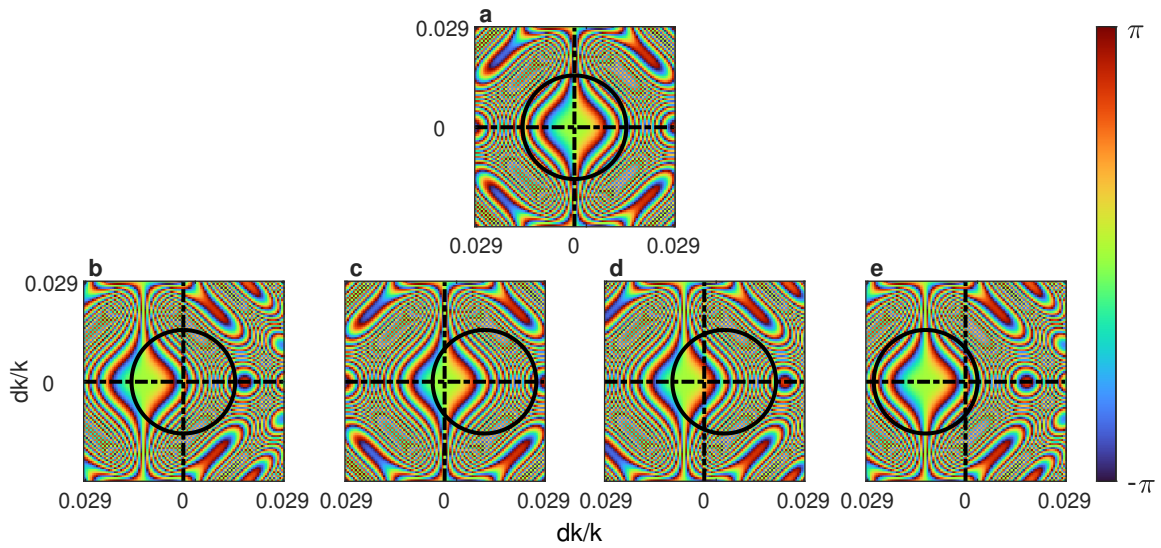

Figure 3.7: Description of the method to generate Airy beams with modified trajectories and intensity peak position. The black circle represents the super-Gaussian aperture (SG). (a) Normally both the phase mask and the SG are coaxially aligned. In our experiments, we produce beams when displacing only the phase mask along the horizontal axis (b), only the SG along the horizontal axis (c), both the phase mask and the SG in opposite directions along the horizontal axis (d) and the phase mask and SG together along the horizontal axis (e).

Results obtained from the misalignments as well as from the Fourier domain and direct field synthesis, are provided in the next chapter.

4. Results

4.1. Quality of generated Airy beams

To determine the quality of produced beams, we compared the experimental data to the simulation, using power ratio as the matrix correspondence indicator. In this case, the power ratio can be calculated as an overlap integral given by:

$$PR = \frac{\iint\limits_S (\sqrt{I_s}.\sqrt{I_e})\, dS}{\iint\limits_S \sqrt{I_s}\, dS \,.\, \iint\limits_S \sqrt{I_e}\, dS}, \tag{4.1}$$

where PR signifies the power ratio, whereas I_s and I_e correspond to simulated and experimentally obtained data intensity profiles, respectively.

To compare the experimental data acquired by the Fourier domain synthesis, the simulated Airy beams were obtained by the two-dimensional Fourier transform of the cubic phase mask, given by Eq. 3.3. Similarly to the Fourier domain synthesis process, the beams were cropped by a circular mask representing the fiber's core. By squaring the resulting electric field distribution, the simulation of an Airy beam intensity profile was generated.

Employing the Fourier domain synthesis, we explored Airy beams with the strength of the cubic phase mask $b = 5$, 10, 15, 20, and 50, respectively, as shown in Fig. 4.1. The best resemblance to the simulation was acquired for parameter $b = 10$, with the PR of 96.61 %. Airy beams, created with the mask of strength $b = 5$, 15 and 20, were also quite similar to the simulation with the PR over 95 %. However, the PR of the Airy beam obtained when employing the phase mask of $b = 50$ was profoundly lower, reaching only 91.51 %. This low PR was caused by the aliasing of the cubic phase mask.

The data obtained utilizing the direct field synthesis were also analyzed by means of the overlap integral. Here, the simulated Airy beams were generated employing equation 3.5. Similarly to the direct field synthesis process, the beams were in a Fourier domain cropped by the fiber's numerical aperture and in a real domain cut by a circular mask representing the fiber's core. The resulting electric field distributions were raised to the power of two to gain the simulated beams' intensity profiles.

Utilizing the method of the direct field synthesis, we also generated Airy beams of the parameter $b = 5$, 10, 15, 20, and 50, achieving the PR above 95 % for all of them as depicted in Fig. 4.2. The highest similarity to the simulation was again obtained for the Airy beam with the parameter b = 10, reaching PR = 96.51 %.

4.2. Propagation of generated Airy beams

One of the typical characteristics of an Airy beam is its curved trajectory, depicted in Fig. 4.3 a. To obtain information about the propagation of synthesized Airy beams, we collected data 40 µm before and after the calibration plane, using a piezo motor attached to the output objective. The step of the motor was 1 µm. The cross-sections through the main lobe of propagating Airy beams, schematically specified by a dashed black line in Fig. 4.3 b, can be seen in Fig. 4.3 c-m. With the increasing value of parameter b,

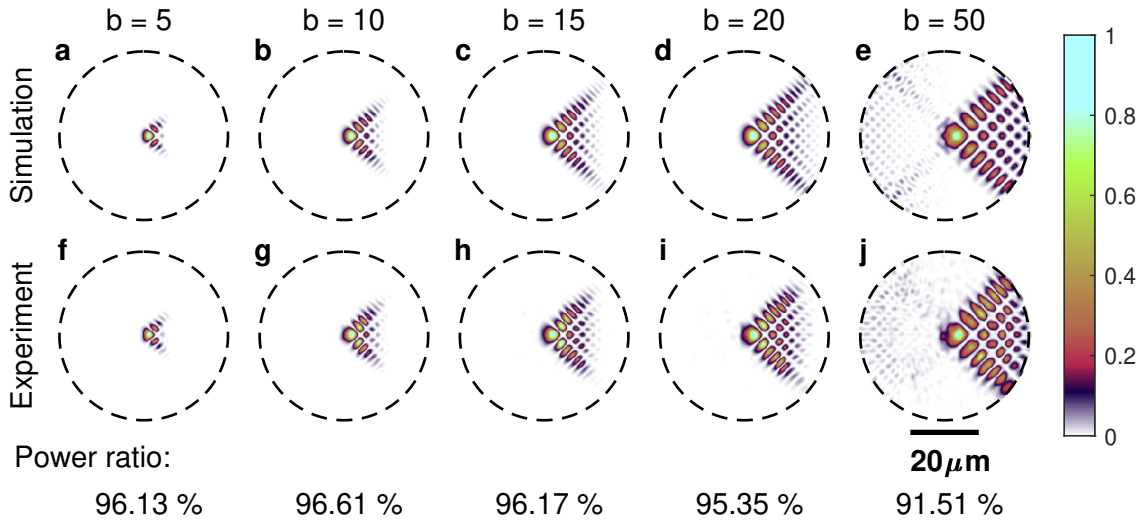

Figure 4.1: In the first row (a-e) are depicted simulated Airy beams. The second row (f-j) contains experimentally obtained Airy beams generated by Fourier domain synthesis, i.e., by masking TM's outputs with the cubic phase mask of strength b = 5, 10, 15, 20, 50. Individual figures are normalized to their maximum and show the intensity distribution of beams at the calibration plane. The black dashed line circle represents the diameter of MMF's core.

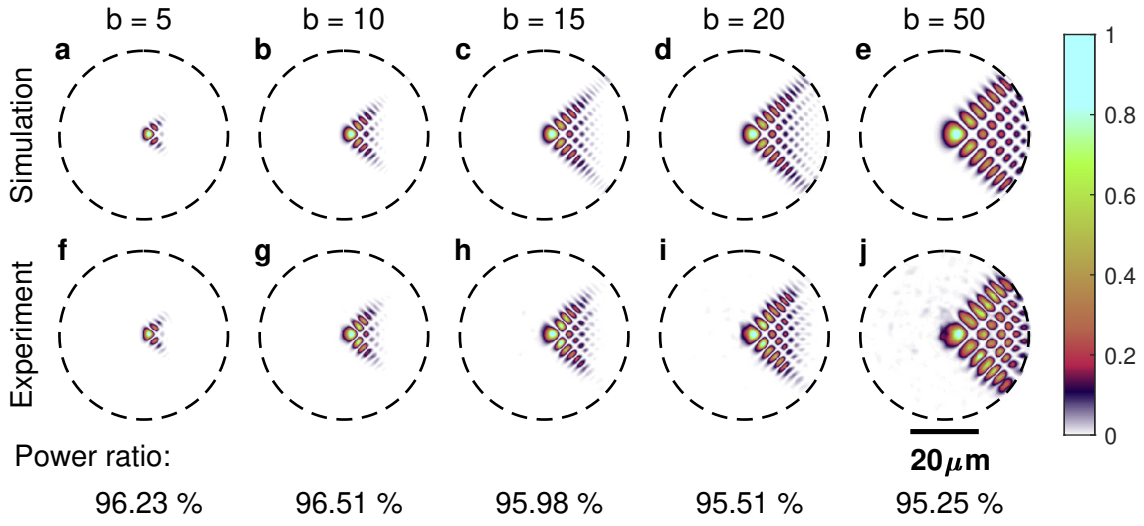

Figure 4.2: In the first row (a-e) are depicted simulated Airy beams. The second row (f-j) contains experimentally obtained Airy beams generated by direct field synthesis, i.e., applying equation number (3) to the TM, using a parameter b = 5, 10, 15, 20, and 50 respectively. Individual figures are normalized to their maximum and show the intensity distribution of beams at the calibration plane. The black dashed line circle represents the diameter of MMF's core.

the trajectory of produced Airy beams was less curved. Furthermore, with higher b, Airy beams had more side lobes; thus, the main lobe carried less energy. The distribution of intensity in individual lobes of an Airy beam created by Fourier domain synthesis with b = 10 is shown in Fig. 4.3 b. Video of propagation and 3D reconstruction of Airy beam

obtained by Fourier domain synthesis with b = 10 can be seen in the supplementary movies 1 and 2.

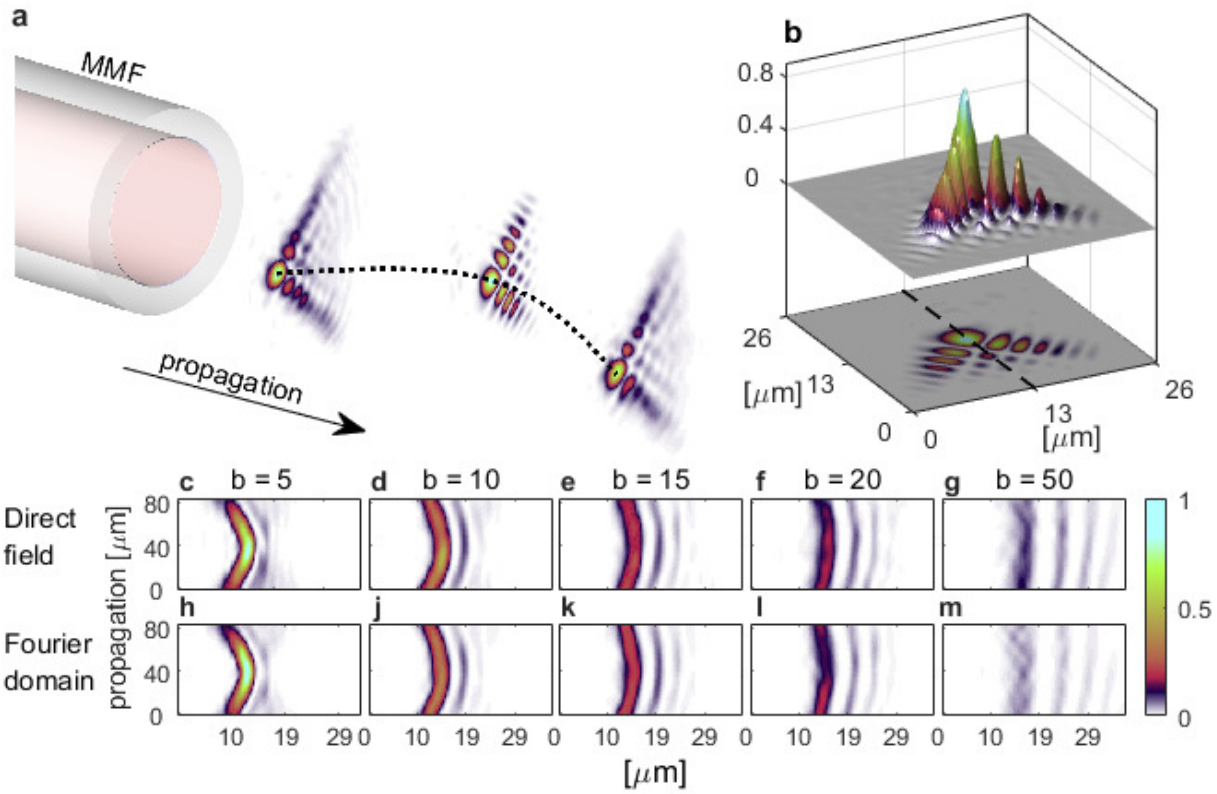

Figure 4.3: (a) Typical curved trajectory of an Airy beam during propagation. (b) Intensity distribution in individual lobes of an Airy beam, generated by Fourier domain synthesis, using the phase mask of strength b = 10. The data were taken in the calibration plane. The dashed black line indicates the position of the row used to construct figures c-f. (c-g) show the cross-sections through the main lobe of propagating Airy beams, created by direct field synthesis, with different b parameters. In comparison, (h-m) depict the cross-sections of propagating Airy beams gained by the Fourier domain synthesis, with different strengths of the cubic phase mask b = 5, 10, 15, 20, and 50.

4.3. Control of the ballistic motion, using the Fourier domain synthesis

As mentioned in Chap. 3.5, to demonstrate the flexibility of the Fourier domain synthesis in modifying the propagation properties of an Airy beam and also to prove that such propagation control can be performed even via the MMF, we were displacing the super-Gaussian aperture or the cubic phase mask of strength b = 10, in a plane transversal to the optical axis. The illustrative scheme, together with a chosen Cartesian coordinate system, is displayed in Fig. 4.4 a.

Fig. 4.4 b, shows a cross-section through the main lobe of propagating Airy beam, obtained when both the super-Gaussian aperture and the phase mask are aligned co-

axially. Unlike the previous experiments, here and in all the following measurements, the data collection started at the calibration plane so that we could capture the whole propagation of the beams with a modified trajectory. Considering this, one can see that the peak intensity of the beam is placed in the calibration plane.

Fig. 4.4 c-d, depicts experimental results obtained after displacement of the cubic phase mask to the positive values of the horizontal axis by 5, 10, 15, and 20 pixels. Set side by side with the original trajectory, shown in Fig. 4.4 b, one can easily see that with a horizontal displacement of the phase mask, we can control the position of starting point as well as the range of propagation, while the intensity peak always appears at the maximum height of the trajectory.

Secondly, we moved the super-Gaussian aperture along the horizontal axis, to its negative side, by the same amount of pixels as in the previous experiment. Results can be found in Fig. 4.4 g-j. Clearly, the beam's trajectory remains the same regardless of the decentering magnitude. However, with a more significant aperture displacement, the intensity peak occurs later during propagation.

Moreover, if we misalign both the mask and the super-Gaussian aperture in the opposite direction of the horizontal axis, we should be able to control the range of propagation as well as the position of the intensity peak [78]. Propagation of the beams obtained by shifting the phase mask and the super-Gaussian aperture in opposite directions so that the total distance between them would be 5, 10, 15, and 20 pixels can be seen in Fig. 4.4 k-n. Here one can see the change in the starting point and the range of propagation, but unlike in [78], the control of intensity peak position is not that apparent. The reason for this lies probably in the super-Gaussian aperture's intensity distribution. In the paper [78], a conventional Gaussian beam intensity was employed, but here we used a flat-top Gaussian beam.

Lastly, we explored the propagation characteristic of beams when displacing the phase mask and the SG aperture together to the positive values of the x-axis by 5, 10, 15, and 20 pixels. Results are depicted in Fig. 4.4 o-r.

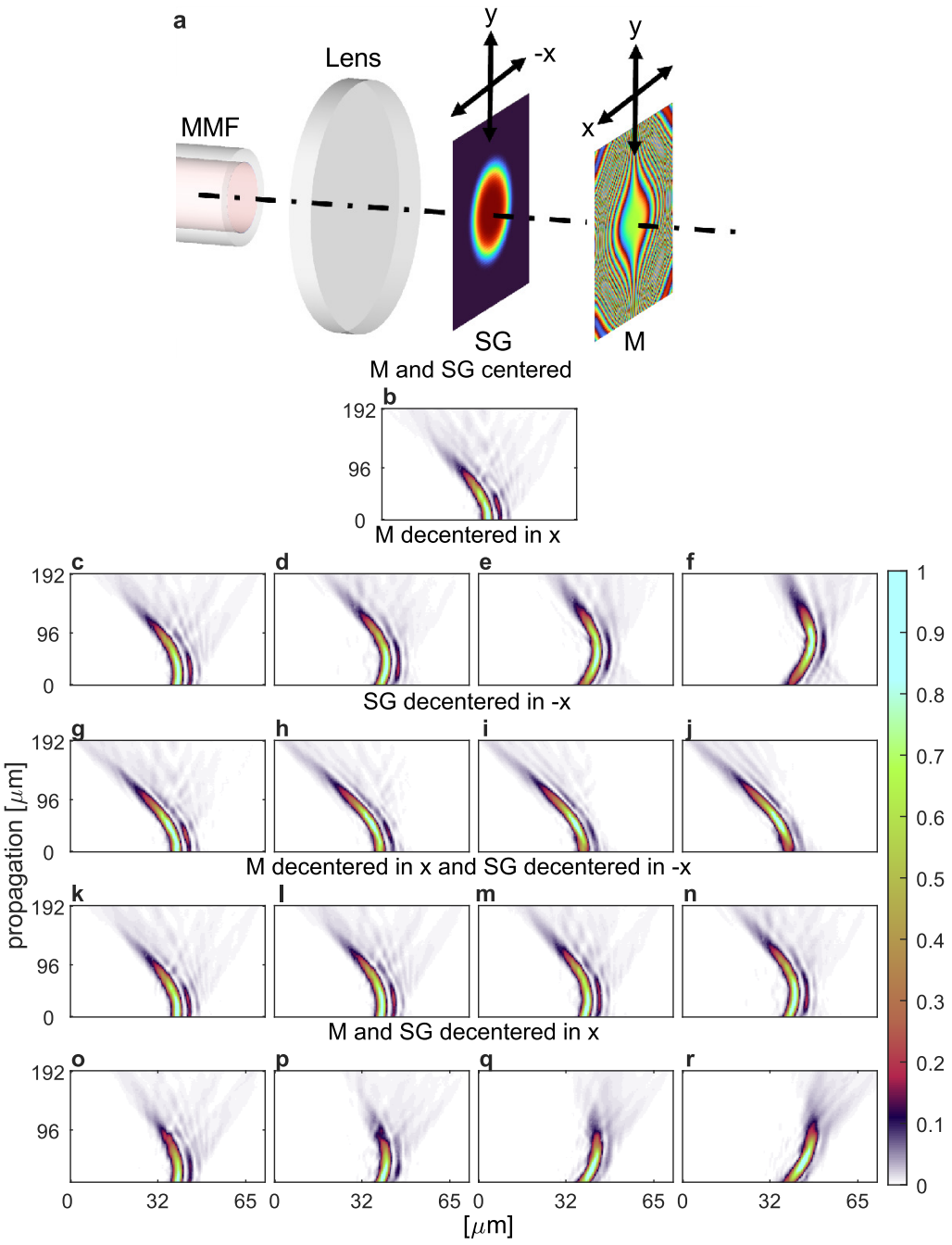

Figure 4.4: (a) Schematic of the multimode fibre (MMF), Fourier lens, super-Gaussian aperture (SG), and the cubic phase mask (M), used to generate Airy beams with modified trajectories. (b) The curved trajectory of the Airy beam when the SG and M are co-axially aligned. (c-f) The trajectory of an Airy beam after shifting the phase mask to positive values of the x-axis by 5, 10, 15, and 20 pixels, respectively. (g-j) The trajectory of the Airy beam after displacing the SG aperture to negative values of the x-axis by 5, 10, 15, and 20 pixels, respectively. (k-n) The trajectory of the Airy beam after misalignment of both the phase mask and SG in opposite directions along the x-axis, each by 2.5, 5, 7.1, and 10 pixels, respectively. (o-r) The trajectory of the Airy beam after shifting both SG and the phase mask in the same direction by 5, 10, 15, and 20 pixels, respectively. The figures (b-r) are normalized to their maximum.

5. Conclusion

The first section of this Master's thesis (Chapter 2) aimed to provide an introduction to the methodology of the novel holographic endoscopy technique. It also covered the fundamental properties, mathematical descriptions, and applications of optical beams, with a specific focus on Gaussian and Airy beams.

The primary goal of this project was to generate an Airy beam through a multimode step-index fiber and determine whether its quality can match the near-perfect foci created through MMF in previous research conducted by Dr. Andre D. Gomes and his colleagues. Chapter 3 presents a detailed description of the optical setup, calibration procedures, and methods employed to generate and control the propagation characteristics of the Airy beams.

To generate the Airy beams, two distinct approaches were employed: the Fourier domain and the direct field synthesis. The direct field synthesis utilized the exact mathematical equation of the 2D finite Airy beam to generate a simulation of desired Airy beam. Employing the simulation together with the information stored in the TM of the MMF, DMD holograms necessary to produce an input field that would, upon propagation through MMF, take the form of the Airy beams were produced. On the other hand, the Fourier domain synthesis involved incorporating a cubic phase mask into the TM and generating the required DMD holograms from this altered TM. The Fourier domain synthesis was also utilized to control the propagation characteristics of the Airy beams. To achieve this, several combinations of shifts to the cubic phase mask or the super-Gaussian aperture were exploited.

Chapter 4 includes the assessment and presentation of the project results. A comparison between the results and simulations revealed the successful generation of high-quality Airy beams at the distal facet of the MMF using both approaches. The Fourier domain synthesis achieved the best PR of 96.61 %, followed closely by the direct field synthesis with the best PR of 96.51 %. Additionally, the propagation of the synthesized Airy beams was recorded, and the ability to control the propagation characteristics of the Airy beam by using the holographic endoscope setup was explored.

This project demonstrates that the recent advancements in the holographic endoscopy technique enable not only the production of simple optical fields, e.g., diffraction-limited foci but also more complex fields, such as Airy beams, with high purity and fidelity. This knowledge holds particular value in the use of the Holographic endoscope in fluorescent microscopy regimes that utilize more complex beams, e.g., structured illumination microscopy (SIM) or stimulated emission depletion microscopy (STED). Employing the Holographic endoscope for in vivo deep-tissue imaging in SIM or STED regimes presents an intriguing challenge for future work.

6. List of Abbreviations

TIR	total inner reflection
SMF	single-mode fibre
MMF	multi-mode fibre
GRIN MMF	graded-index multi-mode fibre
NA	numerical aperture
TM	transformation matrix
SLM	spatial light modulator
LC-SLM	liquid crystal-based spatial light modulator
MEMS	microelectromechanical system
DMD	digital micromirror device
M	cubic phase mask
SG	super-Gaussian aperture
PR	power ratio
SIM	structured illumination microscopy
STED	stimulated emission depletion microscopy

Bibliography

1. GIGAN, S. et al.: Roadmap on wavefront shaping and deep imaging in complex media. *Journal of Physics: Photonics*. 2022, vol. 4, no. 4, p. 73. ISSN 2515-7647.
2. ČIŽMÁR, T.: *Exploiting multimode waveguides for in vivo imaging* [online]. [N.d.]. [visited on 2023-03-04]. Available from: https://spie.org/news/6106-exploiting-multimode-waveguides-for-in-vivo-imaging.
3. HUFELAND, C. W.: *Journal der practischen Arzneykunde und Wundarzneykunst*. Berlin : Wittich, 1806. ISBN 978-0-365-78997-0.
4. HOPKINS, H. H.; KAPANY, N. S.: A Flexible Fibrescope, using Static Scanning. *Nature*. 1954, vol. 173, no. 4392, pp. 39–41. ISSN 1476-4687.
5. BHATT, J. et al.: Harold Horace Hopkins: A Short Biography. *BJU International*. 2010, vol. 106, no. 10, pp. 1425–1428. ISSN 1464-410X.
6. TURTAEV, S.; LEITE, I. T.; ČIŽMÁR, T.: Multimode fibres for micro-endoscopy. *Optofluidics, Microfluidics and Nanofluidics*. 2015, vol. 2, no. 1, pp. 31–35. ISSN 2300-7435.
7. VELLEKOOP, I. M.; MOSK, A. P.: Focusing coherent light through opaque strongly scattering media. *Optics Letters*. 2007, vol. 32, no. 16, pp. 2309–2311. ISSN 1539-4794.
8. VELLEKOOP, I. M.; MOSK, A. P.: Universal Optimal Transmission of Light Through Disordered Materials. *Physical Review Letters* [online]. 2008, vol. 101, no. 12, p. 120601 [visited on 2023-02-20]. Available from DOI: 10.1103/PhysRevLett.101.120601. Publisher: American Physical Society.
9. ČIŽMÁR, T.; MAZILU, M.; DHOLAKIA, K.: In situ wavefront correction and its application to micromanipulation. *Nature Photonics*. 2010, vol. 4, no. 6, pp. 388–394. ISSN 1749-4893.
10. ČIŽMÁR, T.; DHOLAKIA, K.: Shaping the light transmission through a multimode optical fibre: complex transformation analysis and applications in biophotonics. *Optics Express*. 2011, vol. 19, no. 20, pp. 18871–18884. ISSN 1094-4087.
11. LEONARDO, R. D.; BIANCHI, S.: Hologram transmission through multi-mode optical fibers. *Optics Express*. 2011, vol. 19, no. 1, pp. 247–254. ISSN 1094-4087.
12. ČIŽMÁR, T.; DHOLAKIA, K.: Exploiting multimode waveguides for pure fibre-based imaging. *Nature Communications*. 2012, vol. 3, no. 1, p. 1027. ISSN 2041-1723.
13. PAPADOPOULOS, I. N. et al.: High-resolution, lensless endoscope based on digital scanning through a multimode optical fiber. *Biomedical Optics Express*. 2013, vol. 4, no. 2, pp. 260–270. ISSN 2156-7085.
14. CHOI, Y. et al.: Scanner-Free and Wide-Field Endoscopic Imaging by Using a Single Multimode Optical Fiber. *Physical Review Letters* [online]. 2012, vol. 109, no. 20, p. 203901 [visited on 2023-03-02]. Available from DOI: 10.1103/PhysRevLett.109.203901. Publisher: American Physical Society.
15. PLÖSCHNER, M. et al.: Multimode fibre: Light-sheet microscopy at the tip of a needle. *Scientific Reports*. 2015, vol. 5, no. 1, p. 18050. ISSN 2045-2322.

16. MORALES-DELGADO, E. E.; PSALTIS, D.; MOSER, C.: Two-photon imaging through a multimode fiber. *Optics Express*. 2015, vol. 23, no. 25, pp. 32158–32170. ISSN 1094-4087.

17. SIVANKUTTY, S. et al.: Ultra-thin rigid endoscope: two-photon imaging through a graded-index multi-mode fiber. *Optics Express*. 2016, vol. 24, no. 2, pp. 825–841. ISSN 1094-4087.

18. KAKKAVA, E. et al.: Selective femtosecond laser ablation via two-photon fluorescence imaging through a multimode fiber. *Biomedical Optics Express*. 2019, vol. 10, no. 2, pp. 423–433. ISSN 2156-7085.

19. TURCOTTE, R. et al.: Volumetric two-photon fluorescence imaging of live neurons using a multimode optical fiber. *Optics Letters*. 2020, vol. 45, no. 24, pp. 6599–6602. ISSN 1539-4794.

20. LOTERIE, D. et al.: Confocal microscopy through a multimode fiber using optical correlation. *Optics Letters*. 2015, vol. 40, no. 24, pp. 5754–5757. ISSN 1539-4794.

21. GUSACHENKO, I.; CHEN, M.; DHOLAKIA, K.: Raman imaging through a single multimode fibre. *Optics Express*. 2017, vol. 25, no. 12, pp. 13782–13798. ISSN 1094-4087.

22. TRÄGÅRDH, J. et al.: Label-free CARS microscopy through a multimode fiber endoscope. *Optics Express*. 2019, vol. 27, no. 21, pp. 30055–30066. ISSN 1094-4087.

23. CIFUENTES, A. et al.: Polarization-resolved second-harmonic generation imaging through a multimode fiber. *Optica*. 2021, vol. 8, no. 8, pp. 1065–1074. ISSN 2334-2536.

24. TURTAEV, S. et al.: High-fidelity multimode fibre-based endoscopy for deep brain in vivo imaging. *Light: Science & Applications*. 2018, vol. 7, no. 1, p. 92. ISSN 2047-7538.

25. VASQUEZ-LOPEZ, S. A. et al.: Subcellular spatial resolution achieved for deep-brain imaging in vivo using a minimally invasive multimode fiber. *Light: Science & Applications*. 2018, vol. 7, no. 1, p. 110. ISSN 2047-7538.

26. PLÖSCHNER, M. et al.: GPU accelerated toolbox for real-time beam-shaping in multimode fibres. *Optics Express*. 2014, vol. 22, no. 3, pp. 2933–2947. ISSN 1094-4087.

27. MITCHELL, K. J. et al.: High-speed spatial control of the intensity, phase and polarisation of vector beams using a digital micro-mirror device. *Optics Express*. 2016, vol. 24, no. 25, pp. 29269–29282. ISSN 1094-4087.

28. TURTAEV, S. et al.: Comparison of nematic liquid-crystal and DMD based spatial light modulation in complex photonics. *Optics Express*. 2017, vol. 25, no. 24, pp. 29874–29884. ISSN 1094-4087.

29. PLÖSCHNER, M.; TYC, T.; ČIŽMÁR, T.: Seeing through chaos in multimode fibres. *Nature Photonics*. 2015, vol. 9, no. 8, pp. 529–535. ISSN 1749-4893.

30. BOONZAJER FLAES, D. E. et al.: Robustness of Light-Transport Processes to Bending Deformations in Graded-Index Multimode Waveguides. *Physical Review Letters*. 2018, vol. 120, no. 23, p. 233901. ISSN 1079-7114.

31. DU, Y. et al.: Hybrid multimode - multicore fibre based holographic endoscope for deep-tissue neurophotonics. *Light: Advanced Manufacturing*. 2022, vol. 3, no. 3, pp. 408–416. ISSN 2689-9620.
32. SILVEIRA, B. M. et al.: Side-view holographic endomicroscopy via a custom-terminated multimode fibre. *Optics Express*. 2021, vol. 29, no. 15, pp. 23083–23095. ISSN 1094-4087.
33. PIKÁLEK, T. et al.: Suppression of the non-linear background in a multimode fibre CARS endoscope. *Biomedical Optics Express*. 2022, vol. 13, no. 2, pp. 862–874. ISSN 2156-7085.
34. GOMES, A. D. et al.: Near perfect focusing through multimode fibres. *Optics Express*. 2022, vol. 30, no. 7, pp. 10645–10663. ISSN 1094-4087.
35. VETTENBURG, T. et al.: Light-sheet microscopy using an Airy beam. *Nature Methods*. 2014, vol. 11, no. 5, pp. 541–544. ISSN 1548-7105.
36. REMACHA, E. et al.: How to define and optimize axial resolution in light-sheet microscopy: a simulation-based approach. *Biomedical Optics Express*. 2020, vol. 11, no. 1, pp. 8–26. ISSN 2156-7085.
37. SALEH, B. E. A.; TEICH, M. C.: *Fundamentals of Photonics*. USA : John Wiley & Sons, 2019. third edition. ISBN 978-1-119-50687-4.
38. *0.22 NA Silica Core, Glass Clad Multimode Optical Fiber, Step Index* [online]. [N.d.]. [visited on 2023-02-28]. Available from: https://www.thorlabs.com.
39. TUČKOVÁ, T.: *In vivo application of holographic endoscopy*. Brno, 2022. Doctoral thesis. VUT.
40. MOSK, A. P. et al.: Controlling waves in space and time for imaging and focusing in complex media. *Nature Photonics*. 2012, vol. 6, no. 5, pp. 283–292. ISSN 1749-4885, ISSN 1749-4893.
41. CONKEY, D. B. et al.: Genetic algorithm optimization for focusing through turbid media in noisy environments. *Optics Express*. 2012, vol. 20, no. 5, pp. 4840–4849. ISSN 1094-4087.
42. CUI, M.; YANG, C.: Implementation of a digital optical phase conjugation system and its application to study the robustness of turbidity suppression by phase conjugation. *Optics Express*. 2010, vol. 18, no. 4, pp. 3444–3455. ISSN 1094-4087.
43. DRÉMEAU, A. et al.: Reference-less measurement of the transmission matrix of a highly scattering material using a DMD and phase retrieval techniques. *Optics Express*. 2015, vol. 23, no. 9, pp. 11898–11911. ISSN 1094-4087.
44. POPOFF, S. M. et al.: Measuring the Transmission Matrix in Optics: An Approach to the Study and Control of Light Propagation in Disordered Media. *Physical Review Letters* [online]. 2010, vol. 104, no. 10, p. 100601 [visited on 2023-02-19]. Available from DOI: 10.1103/PhysRevLett.104.100601.
45. POPOFF, S. et al.: Image transmission through an opaque material. *Nature Communications*. 2010, vol. 1, no. 1, p. 81. ISSN 2041-1723.
46. POPOFF, S. M. et al.: Controlling light through optical disordered media: transmission matrix approach. *New Journal of Physics*. 2011, vol. 13, no. 12, p. 123021. ISSN 1367-2630.

47. XU, X.; LIU, H.; WANG, L. V.: Time-reversed ultrasonically encoded optical focusing into scattering media. *Nature Photonics*. 2011, vol. 5, no. 3, pp. 154–157. ISSN 1749-4893.

48. JUDKEWITZ, B. et al.: Speckle-scale focusing in the diffusive regime with time reversal of variance-encoded light (TROVE). *Nature Photonics*. 2013, vol. 7, no. 4, pp. 300–305. ISSN 1749-4893.

49. PAPADOPOULOS, I. N. et al.: Focusing and scanning light through a multimode optical fiber using digital phase conjugation. *Optics Express*. 2012, vol. 20, no. 10, pp. 10583–10590. ISSN 1094-4087.

50. BIANCHI, S.; LEONARDO, R. D.: A multi-mode fiber probe for holographic micromanipulation and microscopy. *Lab on a Chip*. 2012, vol. 12, no. 3, pp. 635–639. ISSN 1473-0189.

51. TURTAEV, S.: *Accelerated fibre microendoscopy techniques for in-vivo applications*. Dundee, 2018. Doctoral thesis. University of Dundee.

52. ZHAO, Z.: *High Precision Optical Wavefront Generation Using Liquid Crystal Spatial Light Modulator (LC-SLM)*. IntechOpen, 2021. ISBN 978-1-83881-945-3.

53. ARRIZÓN, V. et al.: Pixelated phase computer holograms for the accurate encoding of scalar complex fields. *Journal of the Optical Society of America A*. 2007, vol. 24, no. 11, p. 3500. ISSN 1084-7529.

54. SONG, Y.; PANAS, R. M.; HOPKINS, J. B.: A review of micromirror arrays. *Precision Engineering*. 2018, vol. 51, pp. 729–761. ISSN 0141-6359.

55. BRENNESHOLTZ, M. S.; STUPP, E. H.: *Projection Displays*. John Wiley & Sons, 2008. ISBN 978-0-470-77091-7.

56. KENNEDY, P.: *DMD spectrometers* [online]. [N.d.]. [visited on 2023-04-06]. Available from: https://ibsen.com/resources/spectrometer-resources/dmd-spectrometers/.

57. LEE, W.-H.: Binary computer-generated holograms. *Applied Optics*. 1979, vol. 18, no. 21, pp. 3661–3669. ISSN 2155-3165.

58. GOORDEN, S. A.; BERTOLOTTI, J.; MOSK, A. P.: Superpixel-based spatial amplitude and phase modulation using a digital micromirror device. *Optics Express*. 2014, vol. 22, no. 15, pp. 17999–18009. ISSN 1094-4087.

59. *Optical resonators and Gaussian beams - Hermite-Gaussian Modes* [online]. [N.d.]. [visited on 2023-05-20]. Available from: http://www.optique-ingenieur.org/en/courses/OPI_ang_M01_C03/co/Contenu_13.html.

60. *Optical resonators and Gaussian beams - Laguerre-Gaussian Modes* [online]. [N.d.]. [visited on 2023-05-20]. Available from: http://www.optique-ingenieur.org/en/courses/OPI_ang_M01_C03/co/Contenu_14.html.

61. SHEN, Y. et al.: Optical vortices 30 years on: OAM manipulation from topological charge to multiple singularities. *Light: Science & Applications*. 2019, vol. 8, no. 1, p. 90. ISSN 2047-7538.

62. KHONINA, S. N. et al.: Bessel Beam: Significance and Applications—A Progressive Review. *Micromachines*. 2020, vol. 11, no. 11, p. 997. ISSN 2072-666X.

63. BERRY, M. V.; BALAZS, N. L.: Nonspreading wave packets. *American Journal of Physics*. 1979, vol. 47, no. 3, pp. 264–267. ISSN 0002-9505.

64. SIVILOGLOU, G. A.; CHRISTODOULIDES, D. N.: Accelerating finite energy Airy beams. *Optics Letters*. 2007, vol. 32, no. 8, pp. 979–981. ISSN 1539-4794.

65. SIVILOGLOU, G. A. et al.: Observation of Accelerating Airy Beams. *Physical Review Letters*. 2007, vol. 99, no. 21, p. 213901.

66. ZHENG, Z. et al.: Optical trapping with focused Airy beams. *Applied Optics*. 2011, vol. 50, no. 1, pp. 43–49.

67. ZHAO, Z.; ZANG, W.; TIAN, J.: Optical trapping and manipulation of Mie particles with Airy beam. *Journal of Optics*. 2016, vol. 18, no. 2, p. 025607. ISSN 2040-8986. Publisher: IOP Publishing.

68. BAUMGARTL, J.; MAZILU, M.; DHOLAKIA, K.: Optically mediated particle clearing using Airy wavepackets. *Nature Photonics*. 2008, vol. 2, no. 11, pp. 675–678. ISSN 1749-4893.

69. POLYNKIN, P. et al.: Curved Plasma Channel Generation Using Ultraintense Airy Beams. *Science*. 2009, vol. 324, no. 5924, pp. 229–232.

70. EFREMIDIS, N. K. et al.: Airy beams and accelerating waves: an overview of recent advances. *Optica*. 2019, vol. 6, no. 5, pp. 686–701. ISSN 2334-2536.

71. ZHU, G. et al.: Obstacle evasion in free-space optical communications utilizing Airy beams. *Optics Letters*. 2018, vol. 43, no. 6, pp. 1203–1206. ISSN 1539-4794.

72. ABDOLLAHPOUR, D. et al.: Spatiotemporal Airy Light Bullets in the Linear and Nonlinear Regimes. *Physical Review Letters* [online]. 2010, vol. 105, no. 25, p. 253901 [visited on 2023-04-02]. Available from DOI: 10.1103/PhysRevLett.105.253901. Publisher: American Physical Society.

73. PIKSARV, P. et al.: Integrated single- and two-photon light sheet microscopy using accelerating beams. *Scientific Reports*. 2017, vol. 7, no. 1, p. 1435. ISSN 2045-2322.

74. NYLK, J. et al.: Enhancement of image quality and imaging depth with Airy light-sheet microscopy in cleared and non-cleared neural tissue. *Biomedical Optics Express*. 2016, vol. 7, no. 10, pp. 4021–4033. ISSN 2156-7085.

75. NAGAR, H. et al.: Non-diffracting beams for label-free imaging through turbid media. *Optics Letters*. 2018, vol. 43, no. 2, pp. 190–193. ISSN 1539-4794.

76. LEITE, I. T. et al.: Three-dimensional holographic optical manipulation through a high-numerical-aperture soft-glass multimode fibre. *Nature Photonics*. 2018, vol. 12, no. 1, pp. 33–39. ISSN 1749-4893.

77. ZHANG, M.; REN, Z.; YU, P.: Improve depth of field of optical coherence tomography using finite energy Airy beam. *Optics Letters*. 2019, vol. 44, no. 12, pp. 3158–3161. ISSN 1539-4794. Publisher: Optica Publishing Group.

78. HU, Y. et al.: Self-accelerating Airy Beams: Generation, Control, and Applications. In: CHEN, Z.; MORANDOTTI, R. (eds.). *Nonlinear Photonics and Novel Optical Phenomena*. New York, NY : Springer, 2012, pp. 1–46. Springer Series in Optical Sciences. ISBN 978-1-4614-3538-9.

79. RUDOLF, B. et al.: Thermal stability of wavefront shaping using a DMD as a spatial light modulator. *Optics Express*. 2021, vol. 29, no. 25, pp. 41808–41818. ISSN 1094-4087.

80. CAO, H. et al.: *Controlling light propagation in multimode fibers for imaging, spectroscopy and beyond*. 2023. Available from arXiv: 2305.09623 [physics.optics].